Endocytic vacuole formation by WASH-mediated endocytosis

Pia Brinkert (1), Lena Krebs (1), Pilar Samperio Ventayol (1), Lilo Greune (2), Carina Bannach (1), Delia Bucher (3), Jana Kollasser (5), Petra Dersch (2), Steeve Boulant (3, 4), Theresia E.B. Stradal (5), Mario Schelhaas (1,6,*)

(1) Institute of Cellular Virology, ZMBE, University of Münster, 48149 Münster, Germany
(2) Institute of Infectiology, ZMBE, University of Münster, 48149 Münster, Germany
(3) Department of Infectious Diseases, Virology, Heidelberg University Hospital, 69120 Heidelberg, Germany
(4) German Cancer Research Center (DKFZ), 69120 Heidelberg, Germany
(5) Department of Cell Biology, Helmholtz Centre for Infection Research, 38124 Braunschweig, Germany
(6) Cells in Motion Interfaculty Center, University of Münster, 48149 Münster, Germany
* Lead contact: schelhaas@uni-muenster.de

Summary

Endocytosis of extracellular or plasma membrane material is a fundamental process. A variety of endocytic pathways exist, several of which are barely understood in terms of mechanistic execution and biological function. Importantly, some mechanisms have been identified and characterized by following virus internalization into cells. This includes a novel endocytic pathway exploited by human papillomavirus type 16 (HPV16). However, its cellular role and mechanism of endocytic vacuole formation remain unclear. Here, HPV16 was used as a tool to examine the mechanistic execution of vesicle formation by combining systematic perturbation of cellular processes with electron and video microscopy. Our results indicate cargo uptake by uncoated, inward-budding pits facilitated by the membrane bending retromer protein SNX2. Actin polymerization-driven vesicle scission is promoted by WASH, an actin regulator typically not found at the plasma membrane. Uncovering a novel role of WASH in endocytosis, we propose to term the new pathway WASH-mediated endocytosis (WASH-ME).

Introduction

Cells internalize extracellular ligands, fluids, plasma membrane lipids and receptors by endocytosis. This is crucial for cellular and organismal homeostasis, signal transduction, intercellular communication, immune response, development and neurotransmission (Schmid and Conner, 2003). Several endocytic mechanisms exist that are distinguished by diverse criteria. Morphologically, cargo is engulfed either by outward membrane protrusions (macropinocytosis, phagocytosis) or by inward budding pits that may or may not display a visible coat in electron microscopy (EM) (e.g. clathrin-mediated endocytosis (CME), glycosphingolipid enriched endocytic carriers (GEEC)) (Heuser and Evans, 1980; Kirkham *et al.*, 2005). The cellular machinery executing endocytic vacuole formation and the destination of endocytic cargo further define the identity of endocytic pathways (Doherty and McMahon, 2009). For instance, macropinocytosis occurs by growth factor-induced, actin-driven protrusions that form large vacuoles upon backfolding with help of the Bin1/Amphiphysin/Rvs (BAR) protein C-terminal binding protein 1 (CtBP1) (Liberali *et al.*, 2008; Lim and Gleeson, 2011). Of the inward budding mechanisms, CME occurs by sequential recruitment of adaptor proteins (AP) such as AP2 and the clathrin coat. Dynamin-2 mediated scission then leads to vacuole formation (McMahon and Boucrot, 2011; Merrifield and Kaksonen, 2014). In contrast, caveolar endocytosis occurs by preassembled coat structures (Pelkmans *et al.*, 2004; Hayer *et al.*, 2010; Stoeber *et al.*, 2016). Another criterium is cargo specificity. For instance, macropinocytosis and CME are responsible for bulk fluid uptake or specific membrane receptor internalization, respectively. A subset of GEEC is specifically responsible for lectin uptake (Lakshminarayan *et al.*, 2014). In addition to the well-established pathways, a number of less well understood endocytic mechanisms have emerged. Only little information is available on which cellular processes they regulate, or on how vesicles are formed, as they are defined by their independence of classical endocytic regulators such as clathrin, caveolin, dynamin-2, or cholesterol (Doherty and McMahon, 2009). Importantly, several of these mechanisms have been identified by following the internalization of viruses such as lymphocytic choriomeningitis virus (LCMV), influenza A virus (IAV), and human papillomavirus type 16 (HPV16) (Rust *et al.*, 2004; Quirin *et al.*, 2008; Mercer, Schelhaas and Helenius, 2010; Schelhaas *et al.*, 2012).

As intracellular parasites, viruses depend on host cells for their life-cycle. This is particularly important during the initial phase of infection termed entry, during which viruses deliver their genome to the site of replication within cells. As virus particles lack locomotive abilities, they strictly rely on cellular transport mechanisms to cross the plasma membrane, the cytosol, or the nuclear envelope. Following viral particles *en route* to the site of replication thus allows to study cellular mechanisms exploited by viruses (Marsh and Helenius, 2006). Most viruses make use of endocytosis to overcome the plasma membrane. Among them is HPV16, a small non-enveloped DNA virus and the leading cause of cervical cancer (de Sanjose *et al.*, 2010; Mirabello *et al.*, 2017). HPV16 initially infects basal keratinocytes of squamous mucosal epithelia, whereas completion of its life cycle requires suprabasal keratinocyte differentiation (Doorbar, 2005). For entry, it utilizes a unique endocytic pathway for which little to no mechanistic information exists (Schelhaas *et al.*, 2012). As viruses strictly hijack existing endocytic mechanisms, the intriguing question remains which cellular cargo targets this pathway. Uptake of HPV16 into cells is slow and asynchronous, with individual virus internalization events occurring over a period of many hours after binding (Schelhaas *et al.*, 2012; Becker *et al.*, 2018). Binding to heparan sulfate proteoglycans (HSPGs) initiates crucial structural changes in the virus capsid that allow transfer to an internalization receptor (complex) to induce uptake (Giroglou *et al.*, 2001; Richards *et al.*, 2006; Selinka *et al.*, 2007; Cerqueira *et al.*, 2013, 2015; Becker *et al.*, 2018). Uptake involves growth factor receptors (Schelhaas *et al.*, 2012; Surviladze, Dziduszko and Ozbun, 2012; Bannach *et al.*, 2020), integrin α6 (Evander *et al.*, 1997; Yoon *et al.*, 2001; Scheffer *et al.*, 2013), tetraspanins cluster of differentiation (CD) 151 and CD63 (Scheffer *et al.*, 2013; Fast *et al.*, 2018), and annexin A2 heterotetramer (Woodham *et al.*, 2012; Dziduszko and Ozbun, 2013). These proteins are thought to constitute specifically functionalized tetraspanin-enriched microdomains termed HPV16 entry platforms that induce uptake and co-internalize with the virus (Raff *et al.*, 2013; Florin and Lang, 2018). After endocytosis, HPV16 traffics through the endosomal system, accompanied by partial capsid disassembly (Smith *et al.*, 2008; Spoden *et al.*, 2008; Bienkowska-Haba *et al.*, 2012). From endosomes, the virus is routed to the trans-Golgi network by retrograde transport (Day *et al.*, 2013; Lipovsky *et al.*, 2013) and reaches its site of replication, the nucleus, after nuclear envelope breakdown during mitosis (Pyeon *et al.*, 2009; Aydin *et al.*, 2014).

HPV16 exploits an endocytic pathway independent of a long list of prominent endocytic regulators including clathrin, caveolin, dynamin and cholesterol. Instead, it depends on sodium/proton exchange, actin polymerization and signaling via epidermal growth factor receptor (EGFR), phosphatidylinositol-4,5-bisphosphate 3-kinase, p21-activated kinase 1, protein kinase C, and Abelson tyrosine-protein kinase 2 (Abl2) (Schelhaas *et al.*, 2012; Bannach *et al.*, 2020). It remains largely elusive how these factors contribute to endocytic vesicle formation. We know, however, that EGFR and Abl2 regulate endocytosis induction and pit maturation, respectively (Bannach *et al.*, 2020). As such, the requirements for HPV16 uptake are somewhat reminiscent of macropinocytosis, during which sodium/proton exchange regulates large actin-driven membrane protrusions to engulf bulk extracellular material (Doherty and McMahon, 2009; Mercer, Schelhaas and Helenius, 2010). However, HPV16 endocytosis typically involves small vesicles of about 60-100 nm diameter that contain single virus particles, and that are generated independently of cholesterol and the classical Rho-like GTPases cell division cycle 42 (Cdc42), rat sarcoma (Ras)-related C3 botulinum toxin substrate 1 (Rac1), and Ras homolog family member 1 (RhoA) (Schelhaas *et al.*, 2012; Bannach *et al.*, 2020). Perhaps, it represents a small-scale version of macropinocytosis, i.e. “micropinocytosis” (Helenius, 2018, 2020).

Here, we used HPV16 as cargo of this unique endocytic pathway to address how vesicles would be mechanistically formed. We demonstrated that HPV16 endocytosis occurred via uncoated vesicles severed from the plasma membrane by actin-related proteins (Arp) 2/3 complex-dependent branched actin polymerization. Interestingly, Arp2/3 complex activation did not involve nucleation promoting factors (NPFs) typically found at the plasma membrane, but the Wiskott-Aldrich syndrome protein (WASP) and suppressor of cAMP receptor (Scar) homologue (WASH), a well-known regulator of endosomal cargo sorting. WASH was recruited to endocytic sites at the same time as sorting nexin 2 (SNX2), a BAR domain protein of the endosomal retromer complex, which supposedly assists in membrane bending during endocytic vesicle formation. Providing insights into the mechanism of a unique endocytic pathway, our findings for the first time conclusively demonstrated a direct involvement of WASH in endocytosis and implicated retromer components in endocytic cargo uptake.

Results

HPV16 endocytosis occurred via uncoated, inward budding vesicles

To assess how this unique mechanism generates endocytic vesicles, we employed HPV16 as trackable cargo in correlative light and EM (CLEM). Our goal was to visualize different stages of endocytic vacuole formation and to address whether potential coat structures were associated with these vacuoles, similar to clathrin-coated pits or caveolae. For this, fluorescent virus particles were correlated with structures on the cytosolic leaflet of plasma membrane sheets analyzed by transmission EM (TEM) of metal replicas (Heuser and Evans, 1980; Sochacki *et al.*, 2014; Bucher *et al.*, 2018). As expected, different stages of clathrin-coated pit formation were readily observable at sites distinct from virus localizations (Figure 1A). For HPV16, about 20% of viruses were associated with no obvious structure, likely representing virus binding to HSPGs prior to engagement of HPV16 entry platforms and endocytosis induction. A considerable proportion (31%) was correlated with dense actin network patches (Figure 1B). These may constitute anchoring structures for tetraspanin microdomains/HPV entry platforms, either prior to or during induction of endocytosis (Schelhaas *et al.*, 2008; Ménager and Littman, 2016). Importantly, inward-budding structures at virus sites were readily observed and classified into stages of vesicle formation in analogy to CME (Figures 1A and 1B). Designated as early stage, 14% of virions were associated with roughened plasma membrane patches representing initial curvature formation (Figures 1A and 1B). Small invaginations (100-150 nm in diameter) were assigned as intermediate stage, and represented pit maturation (13%). Fully rounded invaginations of 80-100 nm (22%) were classified as late-stage endocytic pits ready for scission (Figures 1A and 1B). Notably, all invaginations were devoid of a discernable coat or other regular structures (Figure 1A). Thus, HPV16 endocytosis occurred by a stepwise, inward budding process, in which endocytic vacuoles were formed without observable contribution of a coat structure.

Actin polymerization facilitates HPV16 endocytosis (Schelhaas *et al.*, 2012). Accordingly, perturbation of actin assembly by cytochalasin D (cytoD) reduced HPV16 infection (Figure 1C). To analyze how defective actin assembly impacts the steps of endocytic pit formation, we used CLEM of cytoD-treated cells. As expected, the actin network population was no longer detectable (Figure 1B). However, notably all stages of membrane invaginations were present to a similar extend in cytoD- and untreated samples (Figure 1B). This indicated not only that pit formation was independent of actin polymerization, but also that actin polymerization was expendable for the induction of endocytic pits responsible for HPV16 uptake. In addition, virus-correlated tubular structures devoid of an apparent coat newly appeared in cytoD-treated cells (Figure 1B). In fact, these tubular membrane invaginations were filled with virus particles (Figure 1D). This suggested a fully functional formation of endocytic structures, but a failure in vesicle scission from the plasma membrane. In conclusion, scission but not induction and membrane invagination were facilitated by polymerized or polymerizing actin filaments during HPV16 endocytosis.

Actin polymerization coincided with HPV16 endocytosis

Consistent with actin dynamics aiding vesicle scission in HPV16 uptake, we observed actin signals at the neck of constricted endocytic pits in immunogold labelling EM (Figure 2A). To gain insights into how the dynamics of actin at virus entry sites may facilitate vesicle scission, we employed live cell TIRF microscopy (TIRF-M). In TIRF-M, only the basal plasma membrane is observable. Hence, HPV16 endocytosis into the cell interior was denoted by a rapid loss of virus signal (Figures 2B and 2C, Suppl. Movie 1). Virus signal loss correlated with an increase of filamentous actin signals (Figures 2B and 2C, Suppl. Movie 1) indicating actin polymerization at the time of scission. Detailed analysis of intensity profiles revealed that virus signal loss occurred for about 4 s (Figures 2C and 2D, Suppl. Movie 1). The onset of actin polymerization was somewhat variable. However, the increase in actin signals was on average initiated 7 s prior to virus internalization, peaked just before virus uptake, and decreased thereafter (Figures 2C and 2D, Suppl. Movie 1). The dynamics of actin polymerization resembled dynamin recruitment during scission in CME, starting about 20 s prior to loss of the clathrin signal from the plasma membrane (Figures S1A-S1C, Suppl. Movie 2) (Merrifield *et al.*, 2002). Since dynamin is dispensable for HPV16 endocytosis (Spoden *et al.*, 2008; Schelhaas *et al.*, 2012), similar recruitment profiles suggested that actin functionally replaced dynamin as a scission factor. Moreover, the dynamics of polymerization indicated that polymerized actin did not merely serve as anchor for other scission factors, but was specifically induced for and actively contributed to endocytic vesicle scission as reported for other endocytic mechanisms (Merrifield *et al.*, 2002; Pelkmans, Püntener and Helenius, 2002; Mooren, Galletta and Cooper, 2012).

Branched actin polymerization regulated HPV16 endocytosis

To understand the mechanism of actin polymerization for HPV16 endocytosis, we investigated the involvement of branched versus unbranched actin filaments. Formin-mediated unbranched actin polymerization was perturbed by SMIFH2, a small molecule inhibitor binding the formin homology 2 domain in formins (Rizvi *et al.*, 2009). SMIFH2 treatment dose dependently decreased vesicular stomatitis virus (VSV) infection, confirming the role of formins in actin-dependent CME of VSV

(Figure 3A) (Cureton *et al.*, 2009). In contrast, SMIFH2 did not affect HPV16 infection (Figure 3A). Furthermore, HPV16 infection was largely unaffected by siRNA-mediated depletion of individual formins (Figure S2). However, sequestering the Arp2/3 complex as key regulator of branched actin polymerization by overexpression of the Arp2/3 binding domain of WASP and WASP-family verprolin-homologous protein (WAVE) (Scar-WA) (Machesky and Insall, 1998) strongly reduced HPV16 infection compared to cells expressing a control lacking the Arp2/3 binding domain (Scar-W) (Figure 3B). In line with a requirement of branched actin polymerization, RNA interference (RNAi) with Arp3 expression reduced infection by about 80% (Figure 3C) compared to cells transfected with a non-targeting control (ctrl.). Similarly, vaccinia virus (VV) infection by macropinocytosis (Mercer and Helenius, 2008; Mazzon and Mercer, 2014) was reduced upon Arp3 depletion, whereas Semliki Forest virus (SFV) uptake by actin-independent CME (Marsh and Helenius, 1980; Marsh, Kielian and Helenius, 1984; DeTulleo and Kirchhausen, 1998) was even increased (Figure 3C). Taken together, active branched but not unbranched actin polymerization was crucial for HPV16 infection.

To verify the impact on HPV16 uptake, we employed a *bona fide* virus endocytosis assay. For this, HPV16 covalently labelled with the pH-sensitive dye pHrodo was used, which gives rise to fluorescence only upon delivery to acidic endosomal organelles (Figure 3D) (Ventayol and Schelhaas, 2015; Becker *et al.*, 2018). Depletion of Arp3 reduced virus internalization by about 70% (Figure 3D). Thus, branched actin polymerization was essential for HPV16 endocytosis.

WASH was the major NPF in HPV16 infection

Since the Arp2/3 complex is inherently inactive, how is it activated for virus uptake? Several NPFs with distinct cellular functions and localizations regulate Arp2/3 complex activity (Stradal and Scita, 2006; Rottner, Hänisch and Campellone, 2010). To identify, which NPF acted during HPV16 infection, we employed RNAi. Depletion of the most prominent actin regulators in endocytic processes, neuronal WASP (N-WASP) and WAVE isoforms 1 or 2, (Qualmann and Kelly, 2000; Suetsugu *et al.*, 2003; Chadda *et al.*, 2007), did not alter HPV16 infection (Figures S3A-S3C and S3F). N-WASP RNAi results were confirmed in cells stably expressing a short hairpin RNA (data not shown). Taken together, N-WASP, WAVE1 and 2 were dispensable for HPV16 uptake. Consequently, a potential involvement of NPFs typically not found at the plasma membrane was assessed. Neither depletion of junction mediating and regulatory protein, p53 cofactor (JMY), a regulator of DNA damage response and cell migration (Shikama *et al.*, 1999; Zuchero *et al.*, 2009), nor depletion of WASP homolog associated with actin, Golgi membranes and microtubules (WHAMM), which is involved in the secretory pathway (Campellone *et al.*, 2008), impaired infection with HPV16 (Figures S3D-S3F). However, depletion of WASH, a well-known actin regulator of endosomal cargo sorting (Linardopoulou *et al.*, 2007; Derivery *et al.*, 2009; Duleh and Welch, 2010), strongly reduced HPV16 infection, whereas VV uptake by macropinocytosis was only mildly affected (Figures 4A and S3F). In conclusion, WASH was the major NPF during HPV16 infection rather than NPFs typically found at the plasma membrane.

WASH acted during late stages of HPV16 endocytic vesicle formation

To date, no evidence exists that WASH facilitates endocytic vesicle formation. However, since it was the only NPF important for HPV16 infection, we hypothesized a novel role of WASH in regulating actin polymerization for endocytic vacuole formation. Consistently, silencing of WASH resulted in a strong decrease of HPV16 uptake (Figure 4B). In corroboration, HPV16 infection was completely abrogated in CRISPR/Cas9-derived mouse fibroblast WASH knock-out (KO) cells (NIH-3T3, Figures 4C and S4C). Ectopic expression of wild type WASH rescued HPV16 infection in these cells (Figure 4C and S4A), whereas expression of WASH lacking the WASP-homology 2, central and acidic (WCA) domain crucial for Arp2/3 complex activation did not (Figure S4A). This indicated that WASH was an essential actin regulator during HPV16 uptake. In support, HPV16 infection was also strongly reduced in human osteosarcoma WASH KO cells (U2OS) (Figures S4B and S4C), which not only supported the importance of WASH for HPV16 infection, but also suggested the functional existence of WASH-dependent endocytosis in cells derived from different tissues and species.

After confirming that HPV16 binding to cells was unaffected in WASH KO cells (Figures S4D and S4E), we investigated how loss of WASH would interfere with HPV16 endocytosis by analyzing the morphology of virus-containing pits in ultra-thin section TEM. Compared to wild type cells, the endocytic pits were morphologically unaltered in WASH KO cells, i.e., they were fully formed and partially constricted at the neck (Figure 4D). Thus, early stages of endocytic vesicle formation such as induction and membrane invagination were independent of WASH. Strikingly, the average number of virus containing plasma membrane invaginations more than doubled in the absence of WASH (Figures 4D). Hence, HPV16 endocytosis was stalled at a late stage in WASH KO cells. Taken together, the roles of actin polymerization in vesicle scission, of WASH as the single NPF to promote actin polymerization, and the loss of WASH stalling HPV16 endocytosis at a late stage of vesicle formation strongly suggested that WASH regulated endocytic vesicle scission but not endocytic pit formation.

To directly stimulate vesicle scission, WASH would have to be present at virus endocytosis sites. To probe recruitment of WASH to HPV16 entry platforms marked by HA-CD151 (Scheffer *et al.*, 2013), we employed the proximity ligation assay (PLA) (Söderberg *et al.*, 2006). A small fraction of virus particles co-localized with the PLA signal of WASH and CD151 (Figure S5), indicating that WASH indeed acted at virus entry sites. A limited association of HPV16 with WASH/CD151 structures was expected due to the highly asynchronous virus uptake over many hours, during which only few viruses interact with entry platforms at any given time (Schelhaas *et al.*, 2012; Becker *et al.*, 2018). To more conclusively demonstrate recruitment of WASH to virus entry sites and to gain information on recruitment dynamics, WASH association in relation to uptake of HPV16 was analyzed by live cell TIRF-M. WASH was detected together with virus signals for more than 50 seconds prior to HPV16 uptake and co-internalized with the virus (Figures 4E and 4F, Suppl. Movie 3). Thus, WASH was recruited already early during vesicle formation, although it likely exerted its NPF function only during scission (Figure 4D). To further investigate the stage of WASH recruitment to virus endocytic sites, we performed immunogold labelling of WASH. WASH was observed in close proximity to virus particles bound to flat plasma membrane regions (binding), slightly curved membranes associated with virus particles (early pit), and with fully formed HPV16 endocytic pits (late pit) (Figure 4G). In summary, our data supports a model in which WASH acts in a novel function during endocytosis: WASH was recruited to the plasma membrane early during pit formation, stayed associated during all stages of pit maturation (Figure 4G), and acted at a late stage (Figure 4D) to initiate actin polymerization for vesicle scission during HPV16 endocytosis.

The retromer BAR protein SNX2 facilitated HPV16 endocytosis

How is WASH then recruited to virus entry sites? On endosomes, WASH recruitment occurs by interaction of the WASH regulatory complex with the retromer complex (Gomez and Billadeau, 2009; Harbour, Breusegem and Seaman, 2012; Jia *et al.*, 2012). In line with its well established function in endosomal cargo sorting, the retromer has also been implicated in HPV16 retrograde transport to the Golgi (Lipovsky *et al.*, 2013; Popa *et al.*, 2015; Zhang *et al.*, 2018).

To analyze whether retromer components would play an additional role in HPV16 uptake, we initially used retro-2, a selective inhibitor of retrograde trafficking of e.g. Shiga toxin B from endosomes to the Golgi (Bujny *et al.*, 2007; Popoff *et al.*, 2007; Stechmann *et al.*, 2010). As expected, retro-2 dose-dependently reduced HPV16 infection (Figure 5A) (Lipovsky *et al.*, 2013), while herpes simplex virus 1 (HSV-1) infection was unaffected (Nicola *et al.*, 2005) (Figure 5A). HPV16 binding was unchanged in presence of retro-2 (Figure S6A). Hence, decreased infection was not a consequence of perturbed recycling and reduced receptor presentation. Next, we dissected possible effects of retro-2 on HPV16 endocytosis and retrograde trafficking, respectively. First, we selectively targeted trafficking in an inhibitor swap experiment. HPV16 uptake was allowed in presence of NH_4Cl, a weak base that raises the endosomal pH and prevents onward trafficking of HPV16 (Day, Lowy and Schiller, 2003; Schelhaas *et al.*, 2012). At 12 h post infection (p.i.)., when a large fraction of virus had reached endosomes, NH_4Cl was swapped for retro-2 to prevent retrograde transport. HPV16 infection was dose-dependently decreased (Figure 5B), in line with the requirement for HPV16 endosome-to-Golgi transport (Lipovsky *et al.*, 2013). To assess potential additional effects of retro-2 on HPV16 endocytosis, we analyzed virus uptake in an infectious internalization assay. Cells were infected in presence of retro-2 for 12 h, when extracellular virions were inactivated by a high pH wash and infection by already internalized virions was allowed to continue in absence of retro-2. Uptake of infectious HPV16 was dose-dependently reduced by about 70% in presence of retro-2 (Figure 5C). In conclusion, retro-2 inhibited both retrograde trafficking (Figure 5B) and HPV16 uptake by endocytosis (Figure 5C). To determine the stage of pit formation affected by retro-2 treatment, we performed ultra-thin section TEM. Since retro-2 decreased the number of virus-containing endocytic pits by 90%, it is likely that retro-2 inhibited the initiation of pit formation (Figure 5D). In conclusion, components of the retrograde trafficking machinery already acted during early steps of HPV16 endocytosis.

To specifically address a role for the retromer in either initiation of pit formation or membrane curvature formation, we targeted retromer components by RNAi. The retromer is composed of a cargo-selective complex (CSC) of vacuolar protein sorting (Vps) 26, Vps29, and Vps35, and a dimeric membrane-bending subunit consisting of sorting nexin BAR proteins SNX1/SNX2 and SNX5/SNX6 (Seaman, 2012). As previously observed, RNAi against Vps26, Vps29 and SNX2 strongly reduced infection and suggested that both retromer subunits were required for HPV16 infection (Figures 6A and S6B) (Lipovsky *et al.*, 2013; Siddiqa *et al.*, 2018). As control and to differentiate HPV16 endocytosis from macropinocytosis, depletion of CtBP1, a prominent BAR domain containing regulator of macropinocytosis (Liberali *et al.*, 2008; Valente, Luini and Corda, 2013), did not impair HPV16 infection (Figure 6A).

Since previous work indicates that depletion of Vps29 is expendable for HPV16 uptake but demonstrates an essential role of the CSC in HPV16 endosomal trafficking (Lipovsky *et al.*, 2013, 2015; Popa *et al.*, 2015; Xie *et al.*, 2020), the CSC is unlikely to facilitate HPV16 endocytosis. Recent evidence suggests that retromer BAR proteins can act independent of the CSC on endosomes (Kvainickas *et al.*, 2017; Simonetti *et al.*, 2017; Yong *et al.*, 2020). Hence, we focused our attention on the role of SNX2. While binding of HPV16 to cells was unaffected upon knockdown of SNX2 (Figures S6C and S6D), HPV16 uptake was significantly reduced thereby strengthening a potential role of SNX2 in endocytosis (Figure 6B).

Similar to WASH, a direct involvement of SNX2 in endocytosis necessitates its presence at endocytic sites. During live cell TIRF-M, SNX2 and HPV16 signals co-localized for more than 50 seconds prior to virus uptake and co-internalized (Figures 6C and 6D, Suppl. Movie 4). Thus, SNX2 resembled WASH dynamics during endocytosis. Immunogold labeling confirmed that SNX2 was indeed present at the same endocytic stages than WASH, namely from virus binding to late stages of pit formation (Figure 6E). Thus, these findings indicated a novel function of the retromer protein SNX2 in facilitating HPV16 endocytosis, likely through membrane bending and/or recruitment of WASH to endocytic sites.

Discussion

HPV16 uptake occurs by a unique endocytic mechanism, which is distinguished from other mechanisms predominantly in negative terms, i.e., clathrin-, caveolin-, dynamin-, cholesterol-independent and morphologically distinct from macropinocytosis. This work provides evidence for a mechanistic model, in which HPV16 is internalized by inward budding of uncoated endocytic vesicles. Pit formation is facilitated by recruitment of the membrane bending retromer unit and WASH, the latter of which stimulates branched actin polymerization for scission (Figure 7). Hence, our work not only describes an unexpected direct function of SNX2 and WASH in endocytosis, but also delineates that this mechanism follows a stepwise itinerary similar to CME and distinct from macropinocytosis (Figure 7). Since WASH has neither been described at the plasma membrane nor been attributed to any other endocytic pathway, it defines the molecular identity of the unique endocytic mechanism. Thus, we propose to call this pathway WASH-mediated endocytosis (WASH-ME).

The endocytic landscape includes a variety of pathways, in which endocytic vesicle formation is achieved by different machineries. These pathways typically differ in morphology, key cargos, and molecular features (Doherty and McMahon, 2009). WASH-ME falls in the category of pathways that form endocytic vacuoles by inward budding of the plasma membrane in distinguishable steps. Thus, vesicles are formed by *de novo* assembly of the endocytic machinery in a modular manner, a mode comparable to CME (Figure 7). Vesicle formation is completed by a scission event. In many endocytic pathways, this is mediated by the large GTPase dynamin. During CME, dynamin polymerizes to form a collar that compresses the vesicle neck by an extensively discussed mechanism leading to membrane fission (Hinshaw and

Schmid, 1995; Takei *et al.*, 1995; Sweitzer and Hinshaw, 1998; Morlot and Roux, 2013). In contrast, WASH-ME occurs independently of dynamin (Spoden *et al.*, 2008; Schelhaas *et al.*, 2012) but involves actin polymerization, which coincided with vesicle scission in a timely fashion that resembled dynamin recruitment during CME (Merrifield *et al.*, 2002; Merrifield, 2004). Hence, actin most likely facilitates vesicle scission by a force-driven mechanism rather than as anchoring structure for other scission factors. How actin polymerization creates the force for vesicle scission remains elusive. However, in analogy to observations from CME or endocytosis in *Xenopus* oocytes, actin polymerization towards the vesicle neck may serve to constrict and propel the vesicle away from the plasma membrane (Bement, Sokac and Mandato, 2003; Sokac *et al.*, 2003; Collins *et al.*, 2011).

Endocytic vesicle scission is tightly coupled to membrane remodeling (Dawson, Legg and Machesky, 2006; Shin *et al.*, 2008). This is often coordinated by BAR domain proteins, which sense and stabilize membrane bending by intrinsic curvature (Gallop *et al.*, 2006; Jao *et al.*, 2010; Qualmann, Koch and Kessels, 2011). For instance, SNX9 not only participates in dynamin recruitment (Soulet *et al.*, 2005), but also recruits and directly activates the NPF N-WASP for vesicle scission during CME (Yarar, Waterman-Storer and Schmid, 2007; Shin *et al.*, 2008). Since we demonstrated similar dynamics of SNX2 and WASH at virus entry sites during WASH-ME, perhaps SNX2 aids WASH function in a similar fashion. However, whereas SNX9 and N-WASP are recruited at late stages of CME (Taylor, Perrais and Merrifield, 2011; Kaksonen and Roux, 2018), SNX2 and WASH are already present much prior to vesicle scission. Despite the early recruitment, our findings indicated that WASH promoted actin polymerization only late during vesicle scission. Hence, in contrast to CME, recruitment and activation of the NPF are likely uncoupled in

WASH-ME. How SNX2 recruitment and WASH activation are induced for WASH-ME is unclear. In analogy to their function on endosomes, however, binding of SNX2 to specific phosphoinositides (Zhong *et al.*, 2002; Carlton *et al.*, 2005) and posttranslational modifications of WASH (Hao *et al.*, 2013) are likely involved in their function during WASH-ME. In line with this notion, WASH-ME is controlled by several protein and lipid kinases (Schelhaas *et al.*, 2012; Bannach *et al.*, 2020).

How WASH-ME is induced by ligand-receptor interactions is an intriguing question. In addition to mechanistic insights, it would point to the cellular role of WASH-ME and the cargo it internalizes. Likely, WASH-ME is induced only during specific cell states, as WASH is infrequently observed at the plasma membrane. It is reasonable to assume that HPV16 exploits a pathway that is highly active during infection of target cells. These are basal keratinocytes of the mucosal epidermis that become accessible to the virus upon epidermal wounding (Doorbar, 2005; Roberts *et al.*, 2007; Aksoy, Gottschalk and Meneses, 2017). Wounding and other cellular responses stimulate epithelial to mesenchymal transition and cell migration, which are accompanied by the remodeling of cell-matrix adhesion complexes, such as focal adhesions and hemidesmosomes (HDs) (Jones, Hopkinson and Goldfinger, 1998; Borradori and Sonnenberg, 1999; Webb, Parsons and Horwitz, 2002; Ezratty, Partridge and Gundersen, 2005; Walko, Castañón and Wiche, 2015). To date, little is known about the dynamics of HD remodeling during cell migration, but HD containing plasma membrane domains can be rapidly endocytosed upon detachment from the underlying extracellular matrix (ECM) (Owaribe *et al.*, 1990). Since HDs contain integrin α6 and CD151, which are part of the HPV16 entry platform (Scheffer *et al.*, 2013; Walko, Castañón and Wiche, 2015; Mikuličić *et al.*, 2019), WASH-ME may promote HD uptake during wound healing to aid cell migration and thereby wound closure. Another essential process during wound healing is matrix remodeling. Interestingly, WASH was previously implicated in apical endocytosis of extracellular material in the *Drosophila* airway epithelium during embryogenesis (Tsarouhas *et al.*, 2019). Hence, WASH-ME could also contribute to matrix remodeling as a specialized mechanism for internalization of extracellular material.

While extensive future research will have to address the cellular role of WASH-ME, its role in pathogen invasion may be of considerable interest as well. For instance, WASH is recruited to the plasma membrane during *Salmonella* infection presumably serving as one of several entry pathways (Hänisch *et al.*, 2010). Moreover, WASH regulatory complex protein family with sequence similarity 21 co-localizes with a subset of VV particles in plasma membrane lipid rafts (Huang *et al.*, 2008). Thus, WASH-ME may constitute an important entry route for pathogens. Accordingly, viruses such as IAV and LCMV exploit pathways with endocytic vacuole morphology and mechanistic requirements similar yet not identical to HPV16 endocytosis (Sieczkarski and Whittaker, 2002; Quirin *et al.*, 2008; Rojek, Perez and Kunz, 2008; de Vries *et al.*, 2011).

The identification of SNX2 and WASH marks the beginning of a deeper understanding of the mechanism underlying WASH-ME. Future research will aim to reveal its cellular function, to identify additional components and the functional interplay of the machinery in this uncharacterized new endocytic pathway to better understand the mechanism of WASH-ME.

Limitations of the study

This work describes a novel function of the NPF WASH in regulating actin polymerization for vesicle scission, thereby defining a molecular identity of a unique endocytic pathway exploited by HPV16 for infection. Based on the fact that HPV16 uptake through WASH-ME occurs highly asynchronously over many hours, only very few endocytic events are observable per cell at any given time post infection. Thus, identification of endocytic structures proves to be challenging. For example, colocalization analysis with marker proteins leads to statistically inconclusive results. While dynamic association of cellular proteins with HPV16 during uptake delineated by TIRF-M as well as identification of endocytic pits by EM together with immunogold labelling of cellular proteins demonstrated WASH and SNX2 localization and recruitment to endocytic pits events, the sample size of these experiments is limited if compared to typical colocalization experiments.

Acknowledgements

We thank I. Fels (Institute of Cellular Virology, Münster, Germany) for technical support during virus production and U. Westerkamp as well as M. Dominguez (both Institute of Cellular Virology, Münster, Germany) for assistance with experiments. We are indebted to numerous individuals for sharing valuable reagents as indicated in material and methods. We acknowledge the Infectious Diseases Imaging Platform at the University Hospital Heidelberg, K. Richter from the Core Facility Unit Electron Microscopy at the DKFZ Heidelberg and S. Hillmer from the Electron Microscopy Core Facility of the University Heidelberg for their technical support. This work was supported by funding of the German Research Foundation (DFG) to MS (grants SCHE 1552 6-2 and INST211/817A09), and to SB (grant BO 4340/2-1).

Author contributions

Conceived and designed experiments: PB, LK, PSV, CB, TS, MS; Performed experiments: PB, LK, PSV, LG, CB, DB, JK; Analyzed data: PB, LK, PSV, LG, CB, DB, JK, SB, TS, MS; Resources: PD, SB, TS, MS; Writing: PB, LK, MS with input from the other authors.

Declaration of interests

The authors declare no competing interests.

Figure legends

Figure 1 **HPV16 endocytosis as an uncoated, inward budding mechanism**

(A) HaCaT cells were seeded on HPV16-AF568 bound to ECM, treated with 10 µg/ml cytoD or DMSO and unroofed. Fluorescent virus particles imaged by spinning disk microscopy and depicted in the small insets were correlated with structures identified in TEM images of platinum/carbon replicas of unroofed membranes. Arrowheads indicate endocytic pits. (B) Depicted is the percentage of particles associated with the indicated structure ± variation between the membranes (DMSO: 134 viruses/ 7 membranes; cytoD: 101 viruses/5 membranes). Of note, about 20-25% of particles were not associated with any prominent structure. (C) HeLa ATCC cells were infected with HPV16-GFP in presence of cytoD. Infection was scored by flow cytometry and normalized to DMSO treated controls. The mean of three experiments ± SD is shown. (D) HeLa ATCC cells treated with 10 µg/ml CytoD or left untreated (ctrl.) were infected with HPV16-GFP and processed for ultra-thin section TEM at 6 h p.i.. All scale bars are 100 nm.

Figure 2 **Actin polymerization coincided with HPV16 uptake**

(A) HeLa ATCC cells were infected with HPV16-GFP, subjected to immunogold labeling of actin on ultra-thin cryosections, and analyzed by TEM. Asterisks indicate HPV16 in endocytic pits. Scale bars are 100 nm. (B) HeLa ATCC cells were transfected with lifeact-EGFP, infected with HPV16-AF594 and imaged by live cell TIRF-M at 1 h p.i.. Movies were acquired with 0.5 Hz frame rate for 5 min. HPV16 entry events were identified manually after background subtraction and filtering. The yellow box indicates the virus entry event shown as a kymograph (right) and intensity profile (C). Scale bar is 2 µm. (C) Plotted are the intensity profiles of HPV16 and lifeact (light red/green) as well as moving averages (intense red/green). Values are depicted relative to the half time of virus loss (t = 0). The time points of the onset of actin polymerization (1) and of virus signal loss (2) from the cell surface, as well as of actin peak intensity (3) and of completion of virus uptake (4) were determined manually. (D) Time points were determined for 21 virus entry events as indicated in (C), averaged and are depicted as box plots.

Figure 3 **Branched actin polymerization mediated HPV16 endocytosis**

(A) HeLa ATCC cells were infected with HPV16-GFP or VSV-GFP in presence of the formin inhibitor SMIFH2. Infection was scored by flow cytometry, normalized to solvent treated controls and is depicted as mean ± SD (HPV16: n = 3, VSV: n = 4). (B) HeLa ATCC cells transfected with Scar-W-GFP or Scar-WA-GFP were infected with HPV16-RFP. Infection of transfected cells was analyzed by microscopy, normalized to Scar-W-GFP control cells and is depicted as the mean of three experiments ± SD. (C) HeLa Kyoto cells were depleted of Arp3 and infected with HPV16-GFP, VV-GFP or SFV. Infection was scored by automated microscopy or flow cytometry, normalized to cells transfected with a non-targeting control siRNA (ctrl.) and is depicted as mean ± SD (HPV16/SFV: n = 3, VV: n = 4). (D) Arp3 depletion was followed by infection with HPV16-pHrodo and live cell spinning disk microscopy at 6 h p.i.. Shown are average intensity projections of the HPV16-pHrodo signal with cell outlines (yellow), scale bar is 25 µm. Virus signal intensities per cell were measured using a CellProfiler pipeline and normalized to ctrl. (n = 4, mean ± SD). Knock down levels were analyzed by Western blotting against Arp3.

Figure 4 **WASH associated early, but acted late during HPV16 uptake**

(A) HeLa Kyoto cells were depleted of WASH and infected with HPV16-GFP or VV-GFP. Infection was determined by automated microscopy and flow cytometry and normalized to cells transfected with a control siRNA (ctrl.) (n = 4, mean ± SD.) (B) After depletion of WASH or Arp3, cells were infected with HPV16-pHrodo and imaged live by spinning disk microscopy at 6 h p.i.. Shown are average intensity projections of the HPV16-pHrodo signal with cell outlines (yellow), scale bar is 25 µm. The intensity of virus signal per cell was normalized to ctrl. and is depicted as the mean of three experiments ± SD. (C) EGFP (ctrl.) or EGFP-WASH were expressed in NIH-3T3 wild type and WASH KO cells. Infection with HPV16-RFP was scored by flow cytometry and normalized to wild type cells expressing EGFP (ctrl.). Values are depicted as the mean ± SD (n = 3). (D) NIH-3T3 wild type and WASH KO infected with HPV16-GFP were subjected to ultra-thin section TEM at 6 h p.i.. The number of virus filled plasma membrane invaginations was determined for 43 cells per cell line in two independent experiments. Total pit numbers were normalized to wild type cells and are depicted as mean ± SD. Scale bars are 100 nm. (E) HeLa ATCC cells transfected with EGFP-WASH were infected with HPV16-AF647. Cells were imaged by live cell TIRF-M at 1 h p.i.. Movies were acquired with 0.5 Hz frame rate for 5 min. HPV16 entry events were identified manually after background subtraction and filtering. Shown is a kymograph of the virus entry event highlighted by the yellow box, and the corresponding EGFP-WASH signal. Scale bar is 2 µm. (F) Intensity profiles of HPV16 and WASH (light red/green) as well as moving averages (intense red/green) of the virus entry event shown in (E) depicted relative to the half time of virus loss (t = 0). (G) HeLa ATCC cells were transfected with EGFP-WASH and infected with HPV16. At 6 h p.i., cells were subjected to immunogold labeling of GFP (WASH, 15 nm gold) and actin (10 nm gold) on ultra-thin cryosections analyzed by TEM. Asterisks indicate HPV16 particles, black and white arrowheads indicate WASH staining and the membrane, respectively. Scale bars are 100 nm.

Figure 5 **Components of the retrograde trafficking pathway acted early during HPV16 endocytosis**

(A) HeLa Kyoto cells were treated with retro-2 and infected with HPV16-GFP or HSV-1-GFP. Infection was scored by flow cytometry and normalized to solvent treated controls (n = 3, mean ± SD). (B) HeLa Kyoto cells were infected with HPV16-GFP in presence of 10 mM NH_4Cl. At 12 h p.i., NH_4Cl was washed out and infection was continued in presence of 100 µM retro-2. Infection was scored by flow cytometry at 48 h p.i. and normalized to solvent treated controls. The mean of three experiments ± SD is shown. (C) HeLa Kyoto cells were treated with 100 µM retro-2 and infected with HPV16-GFP. At 12 h p.i., extracellular virus was inactivated by a basic pH wash. Infection was continued in absence of the inhibitor and scored by flow cytometry. Depicted is the fraction of infected cells after the basic wash normalized to DMSO treated cells washed with PBS as the mean of three experiments ± SD. (D) HeLa Kyoto cells were infected with HPV16-GFP in presence of 100 µM retro-2 and subjected to ultra-thin section TEM at 6 h p.i.. Scale bars are 100 nm. The number of virus filled plasma membrane invaginations was determined for 34 and 32 cells in untreated and retro-2 treated cells, respectively, in two independent experiments, normalized to control cells and is depicted as the mean ± SD.

Figure 6 **The retromer protein SNX2 resembled WASH dynamics**

(A) HeLa Kyoto cells were depleted of Vps26a, Vps29, SNX2 or CtBP1 and infected with HPV16-GFP. Infection was scored by automated microscopy and normalized to ctrl. (n = 3, mean ± SD). (B) Cells were depleted of Arp3 or SNX2 and infected with HPV16-pHrodo followed by live cell imaging at 6 h p.i.. Shown are average intensity projections of the HPV16-pHrodo signal acquired by spinning disk microscopy. Cell outlines in yellow were manually created with brightfield images, scale bar is 25 µm. The intensity of virus signal per cell was normalized to ctrl. and is shown as mean ± SD (SNX2: n = 3, Arp3: n = 2). (C) HeLa ATCC cells were transfected with EGFP-SNX2, infected with HPV16-AF647 and imaged live by TIRF-M at 1 h p.i.. Movies were acquired with 0.5 Hz frame rate for 5 min. HPV16 entry events were identified manually after background subtraction and filtering. Shown is a kymograph of the virus entry event highlighted with the yellow box and the corresponding EGFP-SNX2 signal. Scale bars is 2 µm. (D) Intensity profiles of HPV16 and SNX2 (light red/green) as well as moving averages (intense red/green) of the virus entry event shown in (C) depicted relative to the half time of virus loss (t = 0). (E) HeLa ATCC cells were transfected with EGFP-SNX2, infected with HPV16 and subjected to immunogold labeling of EGFP-SNX2 on ultra-thin cryosections analyzed by TEM at 6 h p.i.. Black and white arrowheads indicate SNX2 staining and the membrane, respectively, asterisks mark virus particles. Scale bars are 100 nm.

Figure 7 **Model**

Schematic model of the mechanistic regulation of endocytic vesicle formation during WASH-ME in comparison to CME and macropinocytosis. Additional regulators involved in the latter mechanisms were omitted for clarity.

Supplemental figure legends

Figure S1 **Kinetics of dynamin recruitment during CME resembled actin dynamics during HPV16 uptake** (Related to Figure 2)

(A) HeLa ATCC cells were co-transfected with mRFP-clathrin light chain (CLC) and EGFP-dynamin 2 (Dyn2). Cells were imaged by live cell TIRF-M. Movies were acquired with 0.5 Hz frame rate for 5 min. CME events denoted by CLC signal loss were identified manually after background subtraction and filtering. The yellow box indicates the CME event shown as kymograph. Scale bar is 2 µm. (B) Plotted are the intensity profiles of CLC and Dyn (light red/green) as well as moving averages (intense red/green). Note that due to its additional role in vesicle maturation, Dyn2 was already present early during vesicle formation (Loerke *et al.*, 2009; Taylor, Lampe and Merrifield, 2012). A second wave of recruitment was observed for scission and quantified in (C). (C) The onset of Dyn2 recruitment for scission (1) relative to the half time of CLC loss from the cell surface ($t = 0$) as well as the timepoint of the completion of CLC (3) and Dyn2 (2) signal loss were manually determined from intensity profiles. Values from 10 profiles were plotted.

Figure S2 **Unbranched actin polymerization regulated by formins was not required for HPV16 infection** (Related to Figure 3)

HeLa Kyoto cells were depleted of individual formins and infected with HPV16-GFP. Infection was scored by automated microscopy and normalized to ctrl., siRNAs that reduced cell numbers by more than 80% were considered cytotoxic (†) and excluded from the analysis. Depicted is the mean of three experiments ± SD.

Figure S3 **The NPFs N-WASP, WAVE, WHAMM and JMY were dispensable for HPV16 infection** (Related to Figure 4)

HeLa Kyoto cells were infected with HPV16-GFP after siRNA mediated depletion of N-WASP (A), WAVE1 (B), WAVE2 (C), JMY (D), WHAMM (E). Infection was scored by automated microscopy, normalized to ctrl. and is depicted as the mean ± SD (n = 3). (F) Protein expression levels were determined by Western blotting against the siRNA target proteins.

Figure S4 **The WASH WCA domain was essential for HPV16 infection** (Related to Figure 4)

(A) EGFP (ctrl.), YFP-WASH or YFP-WASH lacking the WCA domain (dWCA) were expressed in NIH-3T3 wild type and WASH KO cells. Cells were infected with HPV16-RFP. Infection was scored by flow cytometry and normalized to wild type cells transfected with EGFP(ctrl.). Values are depicted as mean ± SD of three independent experiments. (B) U2OS wild type and WASH KO cells were infected with HPV16-GFP. Infection was analyzed by flow cytometry and normalized to wild type cells (mean ± SD, n = 8). (C) WASH KO in NIH-3T3 and U2OS cells was confirmed by immunoblotting against WASH. (D) HPV16-AF488 was bound to NIH-3T3 WASH KO cells. Virus pre-incubated with 1 mg/ml heparin was used as a non-binding control. At 2 h p.i., virus binding was measured by flow cytometry. Values are shown as relatives to wild type cells and depicted as mean of three experiments ± SD. (E) Binding of HPV16-AF568 was performed as in (D). After fixation, the actin cytoskeleton was stained with phalloidin-Atto488. Shown are maximum intensity projections of z-stacks acquired by spinning disk microscopy, scale bars are 10 µm.

Figure S5 **PLA indicated WASH recruitment to virus entry sites** (Related to Figure 4)

HPV16-AF488 was bound to ECM. HaCaT cells transfected with the entry platform protein HA-CD151 were seeded on top. Close proximity between WASH and HA-CD151 was detected using a PLA and plasma membrane localization was analyzed by TIRF-M. Scale bars are 2 µm and 0.5 µm.

Figure S6 **Retro-2 treatment and SNX2 knock down did not affect HPV16 binding** (Related to Figures 5 and 6)

(A) Confluent HeLa Kyoto cells were infected with HPV16-AF488 or -AF594 for 2 h in presence of 100 µM retro-2. Pre-incubation of the virus with 1 mg/ml heparin was used as a non-binding control. The intensities of fluorescent HPV16 were determined by spinning disk microscopy and normalized to solvent treated control cells. Depicted are mean values from three experiments ± SD. (B) Depletion of siRNA target proteins was confirmed by Western blotting. (C) HPV16-AF488 was bound to HeLa Kyoto cells depleted of SNX2 for 2 h. Virus binding was determined by flow cytometry. Values are shown as relatives to crtl. (mean of three independent experiments ± SD). (D) HPV16-AF568 was bound to HeLa Kyoto cells depleted of SNX2 as above. Spinning disk microscopy was employed after actin staining with phalloidin-Atto488. Shown are maximum intensity projections of z-stacks, scale bar is 10 µm.

STAR methods

KEY RESOURCES TABLE

REAGENT or RESOURCE	SOURCE	IDENTIFIER
Antibodies		
mouse anti actin (4F7)	BRICS	bsbs300470
rabbit polyclonal anti Arp3	(Steffen *et al.*, 2006)	N/A
mouse monoclonal (11G5a) anti CD151	Bio Rad	MCA1856GA
mouse monoclonal (3) anti CtBP1	Becton Dickinson	612042
rabbit polyclonal anti ERK2 (C-14)	Santa Cruz Biotechnology	sc-154
rabbit polyclonal anti GFP	Abcam	ab290
mouse monoclonal anti HA (16B12)	Covance	MMS-101R
goat polyclonal anti JMY (L-16)	Santa Cruz Biotechnology	sc-10027
primary rabbit antiserum “Lady Di” against SFV E1/2	kind gift from A. Helenius (ETH Zurich, Switzerland), (Singh and Helenius, 1992)	N/A
mouse monoclonal (13) anti SNX2	Becton Dickinson	611308
mouse monoclonal (B-5-1-2) anti tubulin	Sigma-Aldrich	T5168
rabbit polyclonal anti Vps26a	Abcam	Ab137447
rabbit polyclonal anti Vps29	Abcam	Ab98929
rabbit polyclonal anti WASH	kind gift from A. Gautreau (Institut Polytechnique De Paris, Paris, France), (Derivery *et al.*, 2009)	N/A
rabbit polyclonal anti WASH	Atlas Antibodies	HPA002689
rabbit polyclonal anti WAVE1	Sigma-Aldrich	W2142
rabbit polyclonal anti WAVE2 (H-110)	Santa Cruz Biotechnology	sc-33548
rabbit polyclonal anti WHAMM (K-13)	Santa Cruz Biotechnology	sc-136951
goat anti-mouse AF488 IgG	Thermo Fisher Scientific	A-11029
goat anti-mouse AF647 IgG	Thermo Fisher Scientific	A-21235
goat anti-rabbit AF488 IgG	Thermo Fisher Scientific	A-11034
rabbit anti mouse IgG + IgM	Dianova	315-005-048
sheep anti-mouse HRP linked IgG	GE Healthcare	NA931
donkey anti-rabbit HRP linked IgG	GE Healthcare	NA934
Duolink In Situ PLA Probe anti-mouse PLUS	Sigma-Aldrich	DUO92001
Duolink In Situ PLA Probe anti-rabbit MINUS	Sigma-Aldrich	DUO92005
Protein A gold 10 nm	CMC, UMC Utrecht	N/A
Protein A gold 15 nm	CMC, UMC Utrecht	N/A
Bacterial and Virus Strains		
E. coli DH5a	kind gift from A. Helenius (ETH Zurich, Switzerland)	N/A
HPV16-GFP pseudoviruses (PsVs)	(Buck and Thompson, 2007)	N/A
HPV16-RFP PsVs	(Johnson *et al.*, 2009)	N/A
HSV-1-EGFP (17syn$^+$)	kind gift from W. Hafezi (University of Münster, Germany) (Hafezi *et al.*, 2012)	N/A
SFV (prototype strain)	kind gift from A. Helenius (ETH Zurich, Switzerland), (Marsh and Helenius, 1980)	N/A
VSV-GFP (Indiana)	kind gift from A. Helenius (ETH Zurich, Switzerland) (Johannsdottir *et al.*, 2009)	N/A

VV-GFP (Western Reserve)	kind gift from J. Mercer (UCL London, UK), (Mercer and Helenius, 2008)	N/A
Chemicals, Peptides, and Recombinant Proteins		
AGAR 100 Resin kit (Epoxy resin)	Agar Scientific	R1031
Alexa Fluor 488 succinimidyl ester	Thermo Fisher Scientific	A20000
Alexa Fluor 568 succinimidyl ester	Thermo Fisher Scientific	A20003
Alexa Fluor 594 succinimidyl ester	Thermo Fisher Scientific	A20004
Alexa Fluor 647 succinimidyl ester	Thermo Fisher Scientific	A20006
bafilomycin A1	Applichem	A7823
Brij-58	Sigma-Aldrich	P5884
cytochalasin D	Sigma-Aldrich	C8273
glutaraldehyde, EM grade	Polysciences	01909
heparin	Sigma-Aldrich	H4784
Lipofectamine 2000	Invitrogen	11668019
Lipofectamine RNAi max	Invitrogen	13778075
osmium tetroxide	Electron Microscopy Sciences	19100
paraformaldehyde, EM grade	Polysciences	00380
phalloidin-Atto488	Sigma-Aldrich	49409
pHrodo Red succinimidyl ester	Thermo Fisher Scientific	P36600
retro-2	ChemBridge	5374762
RedDot2	VWR	40061-1
ROCK inhibitor	Becton Dickinson	Y-27632
SMIFH2	Sigma-Aldrich	S4826
uranyl acetate	Polysciences	21447
X-tremeGENE™ 9	Merck	XTG9-RO
Critical Commercial Assays		
Duolink In Situ Detection Reagents Red	Sigma-Aldrich	DUO92008
Experimental Models: Cell Lines		
Hamster: BHK-21-Helsinki	kind gift from A. Helenius (ETH Zurich, Switzerland) (Johannsdottir *et al.*, 2009)	N/A
Hamster: BHK-21	kind gift from W. Hafezi (University of Münster, Germany) (Hafezi *et al.*, 2012)	N/A
African green monkey: BSC-40	kind gift from J. Mercer (UCL London, UK), (Brockman and Nathans, 1974)	N/A
Human: HaCaT	(Boukamp *et al.*, 1988)	N/A
Human: HeLa ATCC	ATCC (Manassas, USA)	N/A
Human: HeLa Kyoto	kind gift from L. Pelkmans (ETH Zurich, Switzerland), (Landry *et al.*, 2013)	N/A
Mouse: NIH 3T3	ATCC (Manassas, USA)	N/A
Mouse: NIH 3T3 WASH KOs	this study	N/A
Human: U2OS	German collection of Microorganisms and Cell Cultures (DSMZ, Braunschweig, Germany)	N/A
Human: U2OS WASH KOs	this study	N/A
Non-human, primate: Vero	ATCC (Manassas, USA)	N/A

Human: 293 TT	kind gift from J. Schiller (NIH, Bethesda, USA) (Buck *et al.*, 2005)	N/A
Oligonucleotides		
refer to supplemental table 1 for siRNAs		
single guide RNA (sgRNA) WASH exon 2 (murine, top strand)	GCGACGAGAGGAGGCAATCC	
sgRNA WASH exon 2 (murine, bottom strand)	GGATTGCCTCCTCTCGTCGC	
sgRNA WASH exon 4 (human, top strand)	TCTTCACGGGCGCCCAGGAC	
sgRNA WASH exon 4 (human, bottom strand)	GTCCTGGGCGCCCGTGAAGA	
sgRNA WASH exon 5 (human, top strand)	GTGTGCGTGAGCACCAAGCC	
sgRNA WASH exon 4 (human, bottom strand)	GGCTTGGTGCTCACGCACAC	
murine WASH sequencing primer (forward)	ATAGGCAGAGGGGTGAGTGT	
murine WASH sequencing primer (reverse)	ACACTGGGCATTAGTTGGGT	
M13r primer for TOPO vector	CAGGAAACAGCTATGAC	
Recombinant DNA		
Plasmid: pSpCas9(BB)-2A-GFP (pX458)	Addgene	48138
Plasmid: pEGFP C1_CD151	kind gift from L. Florin (Johannes Gutenberg University Mainz, Germany) (Liu *et al.*, 2007)	N/A
Plasmid: pcDNA3 HA_CD151	this study	N/A
Plasmid: pmRFP C3_Clc	kind gift from A. Helenius (ETH Zurich, Switzerland)	N/A
Plasmid: pEGFP-Dyn2	kind gift from M. A. McNiven (Mayo Clinic, Rochester, USA) (Cao, Garcia and Mcniven, 1998)	N/A
Plasmid: pClneoEGFP	kind gift from C. Buck (NIH, Bethesda, USA) (Buck and Thompson, 2007)	N/A
Plasmid: Lifeact_EGFP-N1	kind gift from R. Wedlich-Söldner (University of Münster, Germany) (Riedl *et al.*, 2008)	N/A
Plasmid: pEGFP C1	kind gift from A. Helenius (ETH Zurich, Switzerland)	N/A
Plasmid: pRwB	kind gift from C. Buck (NIH, Bethesda, USA) (Johnson *et al.*, 2009)	N/A
Plasmid: pEGFP C1_Scar-W-GFP	(Machesky and Insall, 1998)	N/A
Plasmid: pEGFP-C1_Scar-WA-GFP	(Machesky and Insall, 1998)	N/A
Plasmid: pcDNA5_RT-PC-EGFP-SNX2	kind gift from A. Gautreau (Institut Polytechnique De Paris, France), (Helfer *et al.*, 2013)	N/A
Plasmid: pcDNA5_EGFP-WASH	(Derivery *et al.*, 2009)	N/A
Plasmid: pcCM3H1p YFP WASH wild type	kind gift from D. Billadeau (Mayo Clinic, Rochester, USA)), (Gomez and Billadeau, 2009)	N/A

Plasmid: pCMS3H1p YFP WASH dWCA	kind gift from D. Billadeau (Mayo Clinic, Rochester, USA)), (Gomez and Billadeau, 2009)	N/A
Plasmid: p16SheLL	kind gift from C. Buck (NIH, Bethesda, USA) (Buck *et al.*, 2005)	N/A
Software and Algorithms		
Adobe Illustrator	Adobe Inc.	version 16.0.4
Adobe Photoshop	Adobe Inc.	C4, extended version 11.0
Affinity Designer	Serif (Europe) Ltd	version 1.7.3
ApE – A plasmid Editor	M. Wayne Davis (https://jorgensen.biology.utah.edu/wayned/ape/)	version 1.11
BD CellQuest Pro	Becton Dickinson	version 5.2
CellProfiler	(Kamentsky *et al.*, 2011)	version 2.1.1
CellSens Dimension	Olympus	version 2.3
FACSDiva	Becton Dickinson	version 6.1
Fiji (ImageJ)	(Schindelin *et al.*, 2012)	versions 2.0.0/1.50g and 2.1.0/1.53c
FlowJo	Becton Dickinson	versions 8.8.6 and 10.6.1
guavaSoft	Merck	version 3.1.1
iTEMFEI	FEI/Olympus	version 5.2
MATLAB MATLAB InfectionCounter Program	MathWorks (Snijder *et al.*, 2012)	version R2015a, 8.5.0.197613 version blue, release B3
Metamorph (Spinning disk)	Molecular Devices	version 7.7.2
Metamorph (IX71 TIRF)	Molecular Devices	version 7.7.1
Microsoft Excel	Microsoft Corporation	versions 15.41.0 and 16.40
Prism	GraphPad Software, Inc.	version 6.0f
SnapGene Viewer	SnapGene	version 2.6.2
Tecnai software	FEI/Thermo Fisher Scientific	version 3.1.3
Volocity software	PerkinElmer	version 6.3

RESOURCE AVAILABILITY

Lead Contact

Further information and requests for resources should be directed and will be fulfilled by the lead contact, Mario Schelhaas (schelhaas@uni-muenster.de).

Materials Availability

Plasmids generated in this study are available from the lead contact. WASH knock out cell lines described in this study are available from Theresia Stradal (Theresia.Stradal@helmholtz-hzi.de) with a completed Material Transfer Agreement.

Data and Code Availability

All data reported in this paper will be shared by the lead contact upon request. The paper does not report original code. Any additional information required to reanalyze the data reported in this paper is available from the lead contact upon request.

EXPERIMENTAL MODEL AND SUBJECT DETAILS

Cell lines

HeLa ATCC, HeLa Kyoto (both female origin), HaCaT cells (male origin) and non-human, primate Vero cells (female origin) were cultured in high glucose Dulbecco's modified eagle medium (DMEM, D5796 Sigma-Aldrich) supplemented with 10% fetal bovine serum (FBS). 293TT cells (female origin) were grown in DMEM with 10% FBS and 400 µg/µl hygromycin B. U2OS wild type and WASH KO cells (female origin) as well as murine NIH 3T3 wild type and WASH KO cells (male origin) were cultured in DMEM supplemented with 10% FBS and 1% non-essential amino acids (NEAA). Primate, non-human BSC-40 cells (sex unspecified) were grown in DMEM supplemented with 10% FBS, 5% NEAA and 5% sodium pyruvate. Hamster BHK-21 cells (male origin) were cultured in Glasgow's minimum essential medium (GMEM) supplemented with 10% FBS. All cells were cultivated in a humidified atmosphere at 37°C and 5% CO_2 and routinely tested for mycoplasma contamination.

Bacteria strains

Chemocompetent *E. coli* DH5a used for plasmid preparation were grown in lysogeny broth (LB) medium supplemented with antibiotics at 37°C and 210 rpm.

Virus strains

VV-GFP (Western Reserve) containing a fluorescent version of the core protein A5 was propagated and titrated on BSC-40 cells in standard growth medium and purified as described previously (Mercer and Helenius, 2008). HSV-1-EGFP (17syn+) expressing EGFP under control of the cytomegalovirus promoter was propagated on BHK-21 cells and titrated on Vero cells, both grown in GMEM supplemented with 2% FBS, as described previously (Schelhaas *et al.*, 2003; Hafezi *et al.*, 2012). SFV (prototype strain) was propagated and titrated on BHK-21-Helsinki cells as previously described (Marsh, Kielian and Helenius, 1984). Infection was carried out in GMEM supplemented with 10% FBS and 10% Tryptose Broth. VSV-GFP (Indiana) expressing an additional transgene encoding GFP was propagated on BHK-21-Helsinki cells grown in GMEM supplemented with 10 mM HEPES (pH 6.5). At 1 h p.i., GMEM supplemented with 30 mM HEPES (pH 7.3) and 10% Tryptose Phosphate Broth and 1% FBS was added, as previously described (Johannsdottir *et al.*, 2009). The virus was titrated on BHK-21-Helsinki cells grown in RPMI supplemented with 30 mM HEPES (pH 6.5). HPV16 PsVs were produced as described in the method details.

METHOD DETAILS

Cloning and plasmid purification

Cloning of HA-CD151 construct

Lentiviral expression constructs of HA-tagged CD151 were a kind gift from M. Hemler (Dana Farber Cancer Institute and Harvard Medical School, Boston, USA) (Hwang, Takimoto and Hemler, 2019). For subcloning, HA-CD151 was cut from the lentiviral vector using *EcoR*I and *Xba*I for 2 h at 37°C. A pcDNA3 expression vector was cut using the same enzymes and conditions. For purification, both samples were run on a 2% acrylamide gel. The DNA was visualized with ethidium bromide and bands representing the cut pcDNA3 backbone as well as HA-CD151 (insert) were isolated from the gel. Gel extraction was performed with a NucleoSpin Gel and PCR Clean-up kit (Macherey-Nagel). DNA concentrations were determined with help of a 1.5% agarose gel by comparison to the marker bands (Gene Ruler 1 kb DNA ladder, Thermo Scientific). Insert and backbone were ligated by incubation with the T4 ligase overnight at 16°C.

Plasmid purification

Chemocompetent *E. coli* DH5a were incubated with 5 µl ligation product for 10 min on ice. Heat shock was performed by 60-90 sec incubation at 42°C. Immediately afterwards, bacteria were incubated on ice for 5 min before LB medium was added. Bacteria were grown at 37°C and 350 rpm for 30-60 min and plated on LB agar plates with antibiotics using inoculation loops. Plates were incubated overnight at 37°C and inspected for colony growth the next day. For HA-CD151 cloning, several overnight cultures with LB supplemented with antibiotics were inoculated with one colony each. Plasmids were purified using the NucleoSpin Plasmid kit (Macherey-Nagel) and sent for sequencing by Eurofins Genomics (Luxembourg). Sequence analysis was performed with ApE. For use in experiments, plasmids were purified using the NucleoBond Xtra Maxi kit (Macherey-Nagel).

sgRNA design and cloning

sgRNAs were provided by a CRISPR design tool (CRIPR.mit.edu or CCTop). Specifically, the murine gene was disrupted by sgRNAs targeting exon 2 and the human gene by simultaneously targeting exons 4 and 5 (key resources table). Top and bottom strands of sgRNAs were annealed using T4 ligase for 30 min at 37°C and cloned into pSpCas9(BB)-2A-GFP (pX458) by digestion with *Bbs*I and ligation with T4 ligase (6 cycles: 37°C for 5 min, 21°C for 5 min). Residual linearized DNA was removed by treatment with PlasmidSafe exonuclease at 37°C for 30 min. Chemically competent *E.coli* DH5a were transformed with the ligation product as described above.

Generation and characterization of WASH KO cell lines with CRISPR/Cas9

NIH-3T3 and U2OS cells were plated in 6-well plates and maintained in DMEM (4.5 g/L glucose, Invitrogen, Germany) supplemented with 10% (v/v) FBS (Sigma, Germany), 1 mM sodium pyruvate, 1x non-essential amino acids and 2 mM L-glutamine at 37°C in a humidified 7.5% CO2-atmosphere overnight. Cells were genome edited using the CRISPR/Cas9 technology (Ran *et al.*, 2013) to generate WASH KO cell lines. Selected sgRNAs (key resources table) were cloned into pX458 allowing simultaneous expression of sgRNA, Cas9 and selection via EGFP expression as described above. The resulting constructs were transfected into NIH-3T3 or U2OS cells, respectively. Plasmids (1 µg) and X-tremeGene^{TM} 9 (3 µl) were diluted in 100 µl optiMEM, incubated for 30 min at room temperature and added to cells for 16-24 h. Transfection efficiency was monitored using an EVOS® FL Cell Imaging System (Thermo Fisher, Germany). Cells were grown to confluence and subsequently single, GFP-positive cells were sorted into 96-well plates by flow cytometry using a FACSAria II instrument (BD Biosciences) and FACSDiva software. Sorted cells were maintained in growth medium supplemented with penicillin (50 Units/ml)/streptomycin (50 mg/ml) (Thermo Fisher Scientific) and containing 30% conditioned medium and 10 µM ROCK inhibitor (BD Biosciences). After approximately 10 days, clones were picked from single wells and expanded. Derived cell clones were screened for the absence of WASH expression by Western blotting and NIH-3T3 clones lacking detectable amounts of WASH were subjected to genomic sequencing as described (Kage *et al.*, 2017). Cells from confluent 6 cm dishes were trypsinized, pelleted and lysed by overnight incubation in lysis buffer (100 mM Tris pH 8.5, 5 mM EDTA, 0.2% SDS, 200 mM NaCl, 20 mg/ml proteinase K) at 55°C. Nucleic acid extraction was performed by ethanol precipitation. Addition of 700 µl 100% ice cold ethanol was followed by centrifugation at 16,000 x g at 4°C for 30 min. The pellet was washed with 400 µl 70% ice-cold ethanol and samples were dried at 45°C for 20 min. DNA was dissolved in 100 µl deionized water at 4°C overnight and served as template in PCR using GoTaq G2 flexi DNA polymerase. The selected primer pair (key resources table) revealed a PCR product of 330 base pairs. PCR products were examined on 2% agarose gels and appropriate samples purified with a NucleoSpin Gel and PCR clean-up kit (Macherey-Nagel). DNA fragments were cloned into a zero blunt TOPO vector (Zero Blunt TOPO Cloning Kit for Sequencing, Invitrogen) for 5 min at room temperature. After transformation as above, single bacterial colonies were inoculated overnight and plasmid DNA purified using NucleoSpin Plasmid kit (Macherey-Nagel). Sequencing of isolated plasmid DNA was carried out by MWG-Biotech using a standard M13r sequencing primer (key resources table). Clones were examined for frameshift mutations and mono- or biallelic deletions/insertions using SnapGene Viewer software. Mutations or deletions generating stop codons shortly downstream of the target site were defined as 'null' alleles. Cell populations exclusively harboring such alleles out of more than 50 sequencing reactions were selected for further analyses. For WASH targeted clones of murine NIH-3T3 cells, three clones were identified that did not display a wild type allele in more than ten sequencing reactions. All clones showed similar effects on HPV16 infection, thus only one clone is shown in this study. For WASH targeted clones of human U2OS cells no clear sequencing result was obtained probably due to pseudogenes being targeted by sequencing primers.

Western blotting

For analysis of protein amounts after siRNA treatment or CRISPR/Cas9 mediated KO, lysates were prepared in 2x sample buffer (4% SDS, 20% glycerol, 0.01% bromophenol blue, 100 mM Tris HCl (pH 6.8), 200 mM DTT). Samples were denatured for 5 min at 95°C and loaded on polyacrylamide gels. For stacking gels, 5% polyacrylamide was used and separating cells were 6 or 8% for JMY and WHAMM, respectively. All other proteins were separated on 10% gels. Electrophoresis was performed in Laemmli running buffer (0.1% SDS, 25 mM Tris, 192 mM glycine). Proteins were transferred from gels to nitrocellulose membranes for 50 min at 400 mA in pre-cooled transfer buffer (192 mM glycine, 25 mM Tris, 10% methanol). After transfer, membranes were blocked in 5% milk powder (MP) in Tris-buffered saline (TBS) supplemented with 0.2% Tween 20 (TBS-TMP) or in 0.2-3% bovine serum albumin (BSA) for at least 30 min. Primary antibodies were diluted in TBS-TMP or BSA and membranes were incubated for 2 h at room temperature or overnight at 4°C. Three washes with TBS supplemented with Tween 20 (TBS-T) were followed by incubation with anti-mouse or -rabbit secondary antibodies conjugated to HRP diluted in TBS-TMP or BSA. Membranes were washed twice with

TBS-T and once with TBS before the signal from HRP-conjugated antibodies was revealed using enhanced chemiluminescence (ECL) or ECL prime and photographic films.

Virus production

Production of HPV16 PsVs

PsV production was performed as previously described (Buck *et al.*, 2005). A total of 1.8 x 10^7 293TT cells were seeded in 145 mm cell culture dishes. The next day, cells were co-transfected with p16sheLL and the reporter plasmid pClneoEGFP (GFP) or pRwB (RFP). Both plasmids (30 µg each) as well as Lipofectamine 2000 (132.5 µl) were diluted in optiMEM and incubated for 5 min at room temperature. The DNA dilution was added to the Lipofectamine 2000 dilution and samples were incubated for 20 min at room temperature before the transfection mix was added to fresh growth medium in the dishes. At 48 h post transfection, cells were harvested and pelleted. For cell lysis and virus maturation, the pellet was incubated with 0.35% Brij 58, 0.2% Plasmid Safe DNase and 0.2% benzonase for 24 h at 37°C on an overhead rotator. PsVs were purified using a linear 25%-39% OptiPrep density gradient. A PsV fraction at around 30% OptiPrep was collected with a needle and analyzed for virus content and purity by Coomassie staining of SDS-PAGE gels.

Labeling of HPV16 PsVs

HPV16 PsVs were incubated with Alexa Fluor 488, 568, 594 or 647 succinimidyl ester in virion buffer (635 mM NaCl, 0.9 mM $CaCl_2$, 0.5 mM $MgCl_2$, 2.1 mM KCl in PBS, pH 7.6) using a 1:8 molar ratio of L1 to the dye for 1 h on an overhead rotator (Schelhaas *et al.*, 2008; Ventayol and Schelhaas, 2015). Free dye was removed by ultracentrifugation using a 15-25-39% OptiPrep step gradient. The labeled virus between the 25% and 39% OptiPrep fraction was collected with a needle. The PsV concentration was determined by SDS-PAGE and subsequent Coomassie staining. The labeled virus was characterized by binding to glass coverslips and HeLa ATCC cells (Ventayol and Schelhaas, 2015). Labeling of PsVs with pHrodo was achieved following the same protocol. Virus characterization was performed in citric acid buffer (pH 4.4) (Ventayol and Schelhaas, 2015).

Infection experiments

Infection of KO cells

NIH-3T3 (4 x 10^5 cells/well) and U2OS (both 5 x 10^4 cells/well) wild type and WASH KO cells were seeded in 12-well plates. The next day, the growth medium was replaced with 300 µl fresh growth medium and HPV16-GFP was added to result in 20% infection in wild type cells. The virus was bound on a shaker at 37°C. At 2 h p.i., the inoculum was replaced by fresh growth medium and infection was continued. At 48 h p.i., cells were trypsinized and fixed in 4% PFA for 15 min at room temperature. Cells were resuspended in FACS buffer (250 mM EDTA, 2% FBS, 0.02% NaN_3 in PBS) and analyzed for infection (percentage of GFP positive cells) by flow cytometry (FACSCalibur, Becton Dickinson). Gating of infected cells was done with help of uninfected controls. The percentage of infected cells was normalized to the respective wild type cells using Microsoft Excel.

Inhibitor studies

HeLa ATCC cells were seeded in 12-well plates (5 x 10^4 cells/well) about 16 h prior to experimentation. Retro-2 experiments were done with HeLa Kyoto cells (1 x 10^5 cells/well). For HPV16 and HSV-1 infection experiments, small compound inhibitors and solvent controls were diluted in growth medium, while they were diluted in infection medium (RPMI supplemented with 30 mM HEPES, pH 6.5) for VSV infection. Cells were pre-treated with inhibitors or solvent controls for 30 min at indicated concentrations and infected with HPV16-GFP as described above. The inoculum was replaced at 2 h p.i. and infection was continued in presence of the inhibitor. At 12 h p.i., inhibitors were exchanged for 10 mM NH_4Cl/10 mM HEPES in growth medium to reduce cytotoxicity (Schelhaas *et al.*, 2012). Cells were fixed and processed for flow cytometry analysis as described above. For infection with VSV-GFP, the virus was added to the infection medium +/- inhibitor to result in 20% infection in solvent treated controls. VSV-GFP was bound for 2 h on a shaker at 37°C until the inoculum was replaced with 1 ml growth medium. Cells were trypsinized and fixed at 6 h p.i. as described for HPV16. HSV-1 infection was carried out in growth medium containing the inhibitor or the solvent control. The virus was bound at 4°C for 1 h, the medium was exchanged for fresh, warm medium with inhibitors and infection was continued for 5 h at 37°C. Cells were fixed at 6 h p.i. as described before.

To investigate additional effects of retro-2 treatment on HPV16 trafficking, the virus was accumulated in the endolysosomal system by treatment with 10 mM NH_4Cl for the first 12 h of infection (Schelhaas *et al.*, 2012). Then, the inhibitors were replaced by 50/100 µM retro-2 and cells were fixed at 48 h p.i. as described above. All samples were analyzed for infection (percentage of GFP positive cells) by flow cytometry (FACSCalibur, Becton Dickinson). Gating of infected cells was done with help of solvent treated controls to which the percentage of infected cells was normalized.

Infection studies after siRNA-mediated depletion

For siRNA-mediated knockdown, 2 x 10^3 or 2 x 10^4 HeLa Kyoto cells were reverse transfected in 96-well optical bottom plates or 12-well plates, respectively. Transfection was performed using 0.2 µl (96-well) or 0.5 µl (12-well) Lipofectamine RNAi max per well diluted in optiMEM and siRNAs were diluted in optiMEM to reach the working concentration indicated in supplemental table 1. The following procedure and incubation times were as for Lipofectamine 2000. Besides the siRNA against the cellular proteins of interest, the AllStars negative siRNA (ctrl.) was included as a non-targeting control, whereas the AllStars death siRNA was used to test for successful transfection. Moreover, an siRNA targeting GFP was included to suppress the expression of the HPV16-GFP reporter plasmid as a measure for maximal reduction of infection. For RNAi against WASH, cells were transfected twice in 48 h intervals. Cells were infected with HPV16-GFP at 48 h post transfection to result in 20% infection in ctrl. negative transfected controls. In 12-well plates, infection was performed and analyzed by flow cytometry as described above. Absolute infection values were normalized to ctrl. transfected controls. In 96-well plates, the virus was added without prior medium exchange to reduce cell loss. At 48 h p.i., cells were fixed in 4% PFA in PBS and nuclei were stained with RedDot2 for 30 min after permeabilization with 0.1% Triton in PBS. Infection was analyzed by automated microscopy on a Zeiss Axiovert Z.1 microscope equipped with a Yokogawa CSU22 spinning disk module (Visitron Systems). Images were acquired using a 20x objective, a CoolSnap HQ camera (Photometrics) and MetaMorph Software. Cell number and infection were determined using a MATLAB-based infection scoring procedure (Engel *et al.*, 2011). The program detects nuclei and infection signal individually, based on their limiting intensity edges. The edges were filled to objects, which were classified by size. Binary masks of nuclei and infection signal were created and cells were classified as infected if equal or greater than 5% of their nuclei overlapped with infection signal above a certain threshold. In this study, signal twice above the background in the uninfected sample was considered infected. An infection index was obtained for each image and averaged per well (Snijder *et al.*, 2012).

Infection with VV-GFP was carried out in 96-well plates following the same protocol as for HPV16 with the exception that 3 x 10^3 cells were transfected. Virus amounts leading to 20% infection in ctrl. treated controls were used. Cells were fixed at 6 h p.i. and analyzed by automated microscopy, as described above.

For siRNA experiments with SFV, 5 x 10^4 HeLa Kyoto cells were reverse transfected in 12-well plates. Infection was performed by addition of the virus to infection medium (RPMI supplemented with 10% FBS, 10 mM HEPES (pH 7.3)). The virus was bound on a shaker at 37°C. At 2 h p.i., the inoculum was replaced by growth medium. Cells were trypsinized and fixed at 6 h p.i.. Since SFV did not carry a fluorescent reporter plasmid, samples were immunostained for SFV E1/E2 after fixation at 6 h p.i.. Cells were permeabilized with FACS perm (250 mM EDTA, 2% FBS, 0.02% NaN_3, 0.05% Saponin in PBS) for 30 min at room temperature and subsequently incubated with the Lady Di antiserum (Singh and Helenius, 1992) diluted in FACS perm for 2 h at room temperature. Samples were washed thrice with FACS perm and incubated with an anti-rabbit AF488 secondary antibody in FACS perm for 1 h at room temperature. Washing with FACS perm was followed by infection scoring with FACS analysis (FACSCalibur, Becton Dickinson) as described for HPV16. Infection values were normalized to crtl. using Microsoft Excel.

Infection studies in transiently transfected cells

NIH-3T3 wild type and WASH KO cells were seeded in 12-well plates (4×10^4 cells/well). One day later, cells were transfected with plasmids (1 µg) encoding EGFP-WASH or EGFP, YFP-WASH or YFP-WASH dWCA using Lipofectamine 2000 (0.5 µl/well) diluted in optiMEM. Incubation times were the same as for virus preparation. At about 16 h post transfection, cells were infected with HPV16-RFP as described above to result in 20% infection in control cells transfected with GFP. Cells were trypsinized at 48 h p.i., fixed in 4% PFA in PBS and analyzed by flow cytometry (Guava easyCyte, Merck). Final analysis was performed with FlowJo. Transfected cells were gated with help of untransfected controls. Then, the GFP positive population was gated for infection using transfected, but uninfected controls. The percentage of transfected and infected cells (GFP and RFP positive) was normalized to NIH-3T3 wild type cells transfected with the GFP control to obtain relative infection values using Microsoft Excel.

HeLa ATCC cells were transfected with Scar-W and -WA constructs as described above 16-24 h prior to infection. Cells were infected with HPV16-RFP and fixed 48 h p.i. using 4% PFA. Infection was scored using an Olympus IX70 inverted microscope equipped with an electron multiplier CCD camera (EDMCCD, C9100-02, Hamamatsu Photonics K. K.) and a monochromator for epifluorescence excitation. Images were thresholded manually and at least 100 cells were scored for transfection and infection using Fiji.

HPV16 binding assay

For analysis of HPV16 binding by flow cytometry, 5×10^4 NIH-3T3 wild type and WASH KO cells were seeded per well of a 12-well plate. The next day, fluorescently labeled HPV16-AF488 (~1000 particles/cell) was bound to the cells for 2 h on a shaker at 37°C. Cells treated with siRNAs were reseeded at 48 h post transfection (5 x 10^4 cells/well). Virus binding was performed once cells were attached, typically about 6 h post seeding. As a non-binding control, HPV16-AF488 was pre-incubated with 1 mg/ml heparin for 1 h at room temperature prior to binding to cells (Cerqueira *et al.*, 2013). Cells were trypsinized and fixed with 4% PFA. Virus binding was analyzed by measuring the mean fluorescence intensity (geometric mean) of cells in flow cytometry (FACSCalibur). The geometric mean of uninfected cells was subtracted from infected cells and virus binding was normalized to control cells. A similar procedure was applied to measure virus binding to HeLa Kyoto cells depleted of SNX2. Binding was qualitatively assessed for NIH-3T3 wild type and WASH KO cells as well as after SNX2 KD in HeLa Kyoto cells. For this, HPV16-AF568 was bound to these cells as described above. At 2 h p.i., cells were fixed with 4% PFA and stained with 0.1 µg/ml phalloidin-Atto488 diluted in PHEM buffer (60 mM PIPES, 10 mM EGTA, 2 mM $MgCl_2$, 25 mM HEPES, pH 6.9) supplemented with 0.01% Triton X-100 for 30 min. Cells were washed thrice with PBS and mounted on glass slides using AF1 mounting medium. Images were acquired with a Zeiss Axiovert Z.1 microscope equipped with a Yokogawa CSU22 spinning disk module (Visitron Systems) using a 40x objective, a CoolSnap HQ camera (Photometrics) and MetaMorph Software. Z-stacks covering the cell volume were converted to maximum intensity projections using Fiji. Brightness and contrast were adjusted using uninfected samples.

For microscopy-based analysis of retro-2 treated cells, HeLa Kyoto cells were seeded to confluency in a 96-well plate. At least 6 h post seeding, HPV16-AF594 or -AF488 (~1000 particles/cell) were bound to cells in presence or absence of the inhibitor, as above. At 2 h p.i., cells were fixed with 4% PFA and binding was analyzed using a 40x objective of a spinning disk confocal microscope described above. Z-stacks covering the cell volume were converted to sum intensity z-projections using Fiji. The mean fluorescence intensities of HPV16 AF were measured as arbitrary units per field of view. Background intensities measured in uninfected samples were subtracted from raw intensities, which were normalized to solvent treated control cells.

Infectious internalization assay

One day prior to infection, 5 x 10^4 HeLa Kyoto cells were seeded per well of a 12-well plate. Cells were pre-incubated with inhibitors and infected with HPV16-GFP as described above. At 12 h p.i., extracellular virus was inactivated by washing with 1 ml 0.1 mM CAPS buffer (pH 10.5) for 90 sec (Schelhaas *et al.*, 2012; Becker *et al.*, 2018). The cells were washed twice with PBS to remove CAPS and infection was continued in fresh growth medium. To control for inhibitor reversibility, the inhibitor was washed out thrice with PBS without prior CAPS treatment and fresh growth medium was added. At 48 h p.i., cells were fixed and infection was scored by flow cytometry as described above. Infection results were normalized to inhibitor reversibility.

Endocytosis assay with HPV16-pHrodo

Cells were reverse transfected with siRNAs as described above. At 48 h after the first (Arp3, SNX2) or second (WASH) siRNA transfection, HPV16-pHrodo (~1000 particles/cell) was added to 350 µl growth medium and bound for 2 h on a shaker. The inoculum was replaced at 2 h p.i. and cells were imaged live at 6 h p.i. at 37°C and 5% CO_2 in humidified atmosphere using custom made imaging chambers and DMEM high glucose without phenol red supplemented with 10% FBS, 1% L-glutamine and 1% penicillin/streptomycin. Images were acquired on a Zeiss Axiovert Z.1 microscope equipped with a Yokogawa CSU22 spinning disk module (Visitron Systems) using a 40x objective, a CoolSnap HQ camera (Photometrics) and MetaMorph Software. Average intensity projections of confocal slices were generated using Fiji software. Intensity based analysis was performed with CellProfiler (Becker *et al.*, 2018). In brief, the virus signal was enhanced by application of a white top-hat filter. Virus spots were segmented by application of a gaussian filter and maximum correlation thresholding. Virus intensity was then measured in enhanced and original images. Pivot tables (Microsoft Excel) were used to summarize the intensity of spots per condition. These values were normalized to the cell number, which was determined by manual counting from brightfield images. The virus intensity per cell was then normalized to ctrl. treated controls to obtain relative internalization values. Cell outlines were created manually for presentation purposes.

Electron microscopy and CLEM

CLEM

A circular mark used for localization of unroofed cells was generated in the center of coverslips (22 mm diameter) using a diamond knife. For ECM production, 2 x 10^6 HaCaT cells were seeded onto the coverslips placed in a 6-well plate. At 48 h post seeding, ECM was obtained by detaching cells through incubation with 10 mM EDTA/EGTA for 45 min at 37°C, subsequent clapping of the plate and washes with PBS (Culp *et al.*, 2006). HPV16-AF568 was bound to the ECM in 1 ml growth medium/well for 2 h on a shaker at 37°C. HaCaT cells were trypsinized and 12 x 10^5 cells/well were seeded onto the virus bound to ECM. At 1 h post seeding, 10 µg/ml cytoD or DMSO (solvent control) were added. A total of 6 h post seeding, cells were put on ice and washed thrice with cold stabilization buffer (70 mM KCl, 30 mM HEPES (pH 7.4 with KOH), 5 mM $MgCl_2$). For unroofing, the cells were kept on ice and 1 ml cold 2% PFA in stabilization buffer was aspirated with a 1 ml pipette. The pipette was positioned above the marked area in the center of the coverslip and PFA was harshly released onto the cells. The coverslip was then rapidly transferred to a new well containing cold 2% PFA in stabilization buffer to avoid sedimentation of cell debris on the unroofed membrane. Membrane sheets were fixed for 10 min at 4°C. Samples were mounted in custom-made imaging chambers and imaged in PBS at a Nikon Ti Eclipse microscope equipped with a PerkinElmer UltraVIEW VoX spinning disk module. Images were acquired using a 60x objective, an Orca Flash 4 camera (Hamamatsu) and Volocity software (PerkinElmer, version 6.3). Montages of 10 x 10 images and 10% overlap were acquired around the center of the marked area. The unroofed membranes were prepared for EM by fixation with 2% glutaraldehyde (GA) in PBS overnight at 4°C. After two washes with water, samples were incubated with 0.1% tannic acid for 20 min at room temperature and subsequently washed with water. Contrasting was performed with 0.1% uranyl acetate (UAC) for 20 min at room temperature. After three washes with water, samples were dehydrated with a series of ethanol solutions (15%/30%/50%/70%/80%/90%/100%). Coverslips were incubated with each solution for 5 min, incubation with 100% ethanol was repeated thrice. Samples were dried using hexamethyldisilazane (HDMS). After 5 min incubation at room temperature, fresh HDMS was added and samples were incubated for further 30 min at room temperature. Coverslips were dried and coated under vacuum using a Balzers BAF301 device (former Balzers AG, Liechtenstein). A first layer of platinum was applied at an angle of 11°C while rotating. A second layer of carbon was applied at an angle of 90° while rotating. Coverslips were cut to fit on

EM grids before 5% hydrofluoric acid were used to separate the metal replica from the glass. Replicas were extensively washed with water prior to transfer to glow discharged, formvar coated EM grids. Replicas were imaged with a phase contrast microscope for orientation. Intact membranes associated with virus particles were manually selected based on overlays of images from fluorescence and phase contrast microscopy and imaged at a TEM (Jeol JEM-1400, Jeol Ltd., Tokyo, Japan, camera: TemCam F416; TVIPS, Gauting, Germany). Membrane sheets were imaged using montages of 5 x 5 images and 15% overlap. Fluorescence and EM images were initially overlaid manually using Photoshop, then the Fiji plugin Landmark Correspondences (Saalfeld and Tomancák, 2008) was used for transformation of the fluorescence image according to the EM image using three manually identified landmarks. For analysis, HPV16 was identified manually based on the fluorescent signal and classification was done by visual evaluation of associated structures in TEM images. At total of 134 and 101 membrane associated virus particles in DMSO (7 membranes) and cytoD (5 membranes) treated cells were analyzed, respectively.

Ultra-thin section EM

Samples for ultra-thin section EM were prepared and analyzed as described previously (Bannach *et al.*, 2020). A total of 1-2 x 10^5 NIH 3T3 wild type, WASH KO and HeLa Kyoto cells or were seeded in 3 cm dishes. Two days post seeding, cells were either pretreated with inhibitors for 30 min or were left untreated. Cells were infected with 40 µg HPV16 PsVs in 1 ml growth medium. At 6 h p.i., cells were fixed in 2.5% GA in PBS (pH 7.2) for 10 min at room temperature. A second fixation was performed with cold 2.5% GA at 4°C overnight. Cells were washed thrice with PBS, post-fixed with 1% OsO_4 in ddH_2O for 1 h and washed twice with ddH_2O at room temperature and at 4°C for 20 min, respectively. Block contrasting was performed with 0.5% UAC in ddH_2O at 4°C overnight. Cells were washed thrice with ddH_2O and dehydrated using ascending graded alcohol series. Detaching and dehydrating with propylene oxide were followed by incubation with propylene oxide and epoxy resin (1:3, 1:1, 3:1) for 2 h each, before cells were incubated with pure epoxy resin for 3 h and embedded in BEEM capsules. The resin was allowed to polymerize at 60°C for three days before 60 nm ultra-thin sections were cut and counterstained with uranyl acetate and lead. Samples were imaged at a 80 kV on a Tecnai 12 electron microscope (FEI) using an Olympus Veleta 4k CCD camera or Ditabis imaging plates. Images were contrast enhanced and cropped using Adobe Photoshop CS4. The total number of endocytic pits per cell was determined for 31 and 43 cells in wild type and WASH KO cells, respectively, in two independent experiments. Only endocytic pits containing virus(es) were counted, since HPV16 pits are hardly distinguishable from uncoated pits from other endocytic pathways without further staining. Pit numbers were normalized to wild type cells.

Immunogold labeling

HeLa ATCC cells (2-3 x 10^5 cells) were seeded in 6 cm dishes. The next day, cells were transfected with a plasmid encoding EGFP-WASH or EGFP-SNX2 (7 µg) using Lipofectamine 2000 (3.5 µl) according to the manufacturer's instructions or left untransfected. At 48 h post transfection, cells were infected with 80 µg HPV16 PsVs and incubated for 6 h at 37°C until pre-fixation by addition of 4% formaldehyde in 0.1 M phosphate buffer (pH 7.2) to the culture medium (1:1 ratio) for 5 min. Then, cells were fixed in 2% formaldehyde, and 0.2% GA in 0.1M phosphate buffer (pH 7.2). Samples were processed for TEM as previously described (Humbel and Stierhof, 2009). In brief, cells were quenched by incubation in 0.1% glycine in 0.1 M PB (2 x 30 min), washed thrice in 0.1 M PB for 30 min and scraped with 1% gelatin.

After centrifugation, the gelatin was replaced with 12% gelatin and cells were infused at 37°C. Cells were cooled down on ice and the gelatin-cell pellet was cut into small blocks that were infused with 2.3 M sucrose overnight at 4°C. The blocks were mounted on specimen carriers and frozen in liquid nitrogen. Ultra-thin cryosections were prepared according to Tokuyasu (Tokuyasu, 1980). In brief, ultra-thin cryosections of 50 nm thickness were prepared with an EM UC6/FC6 ultramicrotome (Leica Microsystems). Sections were collected in a sucrose-methylcellulose mixture and stored on TEM grids at 4°C until further processing. Methylcellulose was melted and sections were washed five times with 20 mM glycine in PBS. Quenching was followed by blocking with 1% BSA for 3 min. Cells were then incubated with a GFP-antibody for 30 min, washed 6 times with 0.1% BSA in PBS and incubated with protein A gold 15 nm for 20 min. Sections were rinsed 10 times with PBS and re-fixed in 1% GA in PBS (pH 7.2). For double labeling, the sections were quenched, blocked and immunostained with an actin antibody as described above. Then sections were incubated with a rabbit anti-mouse bridging antibody followed by 6 washes with 0.1% BSA in PBS and incubated with protein A gold 10 nm (1:50). Sections were rinsed 10 times with PBS and re-fixed in 1% GA in PBS, pH 7.2. Sections were rinsed 10 times with ddH_2O and contrasted with uranyl acetate for 6 min (pH 7). After one wash with ddH_2O, cells were embedded in an uranyl acetate-methylcellulose mixture (pH 4) for 10 min. After looping out with filter paper, sections were dried and images were acquired as above.

Fluorescence microscopy

CLC and virus internalization analysis by live cell TIRF microscopy

HeLa ATCC cells were seeded on coverslips in 12-well plates (5 x 10^4 cells/well) one day prior to transfection. Cells were transfected with plasmids encoding lifeact-EGFP,

EGFP-WASH, EGFP-SNX2, mRFP-CLC or EGFP-Dyn2 as described above. For internalization analysis, fluorescently labeled virus (HPV16-AF594/AF647) was bound at 37°C at about 18 h post transfection. At 1 h p.i., coverslips were mounted in custom-made imaging chambers. Cells were imaged at 37°C and 5% CO_2 in humidified atmosphere in DMEM without phenol red supplemented with 10% FBS, 1% L-glutamine and 1% penicillin/streptomycin. Time lapse movies of cells expressing lifeact-EGFP were acquired with a 60x TIRF-objective on an Olympus IX70 microscope equipped with a TIRF condenser and an electron multiplier CCD camera (EDMCCD, C9100-02, Hamamatsu Photonics K. K.) using MetaMorph software (Molecular Devices) (Visitron Systems). All other time lapse movies were acquired using a 100x TIRF-objective at an Olympus IX83 microscope equipped with a four-line TIRF condenser and an EMCCD camera (iXon Ultra 888, Andor Oxford Instruments) using CellSens Dimensions software (Olympus). Movies were acquired with 0.5 Hz frame rate for 5 min. HPV16 entry events were identified manually and the intensity of fluorescent proteins at virus entry sites was analyzed after rolling ball background subtraction and filtering (mean intensity filter) with Fiji. Kymographs, intensity profiles along a manually drawn line through the virus/clathrin signal over time, were generated with Fiji after background subtraction and filtering. Intensity profiles measured with Fiji using a circular region of interest, were processed by min/max normalization and aligned by setting the half time of virus internalization to 0 s. Profiles were plotted with Microsoft Excel. Moving averages of signals are shown as a trendline (period 4-20). The time points of recruitment onset, maximal signal or signal loss were manually determined relative to the half time of internalization and box plots were generated with GraphPad Prism. Cells co-transfected with CLC and Dyn2 were analyzed the same way at about 16 h post transfection. Movies were compressed to 20 fps and PNG.

Proximity ligation assay

For ECM production on coverslips, 5 x 10^5 HaCaT cells were seeded per well of a 12-well plate and cultivated at 37°C for 2 days. Additionally, 7 x 10^4 HaCaT cells were seeded per well and transfected the next day with a plasmid encoding HA-CD151. The procedure was the same as for infection studies with transfected cells, but 0.4 µg DNA and 1 µl Lipofectamine 2000 per well were used. ECM on coverslips was obtained by detaching cells with 0.5 ml 10 mM EDTA/EGTA as described above. HPV16-AF488 (~1000 particles/cell) was bound to the ECM in 400 µl growth medium on a shaker at 37°C. At 2 h post binding, HaCaT cells expressing HA-CD151 were trypsinized and transferred onto the virus bound to ECM. Cells were allowed to attach for 5 h and fixed in 2% PFA in PBS for 10 min at 4°C. Cells were permeabilized with 0.2% Brij 58 in PBS for 10 min at room temperature prior to blocking in 1% BSA in PBS for 30 min at room temperature. Primary antibody staining against HA (1:10,000) and WASH (1:500) was carried out in a wet chamber overnight at 4°C. Next, cells were incubated with anti-mouse PLUS and anti-rabbit MINUS Duolink PLA probes diluted 1:5 in 1% BSA in PBS for 1 h at 37°C in a humidity chamber. Duolink In Situ Detection Reagents Red were used for further sample processing. For ligation of PLA probes, 1.25 U ligase per sample were added to the corresponding ligation buffer diluted in ddH_2O. The cells were incubated in at wet chamber for 30 min at 37°C followed by two washes with wash buffer B (2 min, room temperature). Amplification was performed with 6.25 U polymerase and Duolink Amplification Red (1:5) diluted in ddH_2O in a wet chamber at 37°C for 100 min. Cells were washed twice for 10 min with wash buffer B at room temperature followed by a quick wash with 0.1x wash buffer B in ddH_2O. As a counterstain, HA (CD151) was detected with an anti-mouse AF647 antibody, which was diluted 1:2000 in 1% BSA in

PBS. Samples were transferred to custom made imaging chambers. Images were acquired with a 100x TIRF-objective at an Olympus IX83 microscope equipped with a four-line TIRF condenser and an EMCCD camera (iXon Ultra 888, Andor Oxford Instruments) using CellSens Dimension software (Olympus).

Quantification and statistical analysis

Information on data representation (mean ± SEM) and n can be found in the figure legends. Statistical significance was determined using unpaired t-tests conducted with GraphPad Prism. A P-value below 0.05 ($P < 0.05$) indicated a significant difference, denoted by asterisks in the figures (* $P \leq 0.05$, ** $P \leq 0.01$, *** $P \leq 0.001$). If not specifically indicated, differences were not significant.

Supplemental movie legends

Supplemental movie 1 **Actin polymerization coincided with HPV16 internalization (**Related to Figure 2)

HeLa ATCC cells transfected with lifeact-EGFP (actin, green) were infected with HPV16-AF594 (HPV16, red) and imaged by live cell TIRF-M at 1 h p.i.. Movies were acquired with 0.5 Hz frame rate for 5 min and processed by background subtraction and mean filtering. Shown is the virus entry event characterized in Figure 2. Depicted are 200 frames corresponding to 1:40 min real time at a compression rate of 20 frames per seconds (fps). The virus internalizing during the movie is highlighted by a circle. Scale bar is 200 nm.

Supplemental movie 2 **Dynamin recruitment during CME resembled actin dynamics during HPV16 endocytosis (**Related to Figure S1)

HeLa ATCC cells co-transfected with mRFP-clathrin light chain (CLC, red) and EGFP-dynamin 2 (Dyn2, green) were imaged by live cell TIRF-M. Movies, acquired with 0.5 Hz frame rate for 5 min, were processed by background and mean filtering. Shown are 1:40 min (200 frames) of the CME event characterized in Figure S1 at a compression rate of 20 fps. The CLC of interest is marked by a circle. Scale bar is 200 nm.

Supplemental movie 3 **WASH co-internalized with HPV16** (Related to Figure 4)

EGFP-WASH (WASH, green) was expressed in HeLa ATCC cells, which were subsequently infected with HPV16-AF647 (HPV16, red). Movies were acquired by live cell TIRF-M at 1 h p.i. for 5 min at 0.5 Hz frame rate. The virus entry event highlighted by a circle was characterized in Figure 4. Shown are 1:14 min

(150 frames) with a compression rate of 20 frames per second. The movie was processed by background subtraction and mean filtering. Scale bar is 200 nm.

Supplemental movie 4 **SNX2 co-internalized with HPV16** (Related to Figure 6) HeLa ATCC cells were transfected with EGFP-SNX2 (SNX2, green) and infected with HPV16-AF647 (HPV16, red). Movies of live cells were acquired with 0.5 Hz frame rate for 5 min at a TIRF-M. An excerpt of 1:14 min (150 frames) compressed to 20 frames per second is shown after background subtraction and mean filtering. The virus particle of interest is marked with a circle. Scale bar is 200 nm.

Supplemental table 1 (siRNA)

siRNA	working concentration (nM)	Qiagen identifier
AllStars death	10	SI04381048
AllStars negative (siCtrl.)	10/20/50	SI03650318
Arp3 siRNA_1	10	Hs_ACTR3_5
Arp3 siRNA_2	10	Hs_ACTR3_8
CtBP1 siRNA_1	10	Hs_CTBP1_5
CtBP1 siRNA_2	10	Hs_CTBP1_6
Formin 1 siRNA_1	10	Hs_FMN1_5
Formin 1 siRNA_2	10	Hs_FMN1_6
Formin 1 siRNA_3	10	Hs_FMN1_7
Formin 2 siRNA_1	10	Hs_FMN2_12
Formin 2 siRNA_2	10	Hs_FMN2_7
Formin 2 siRNA_3	10	Hs_FMN2_9
FNL2 siRNA_1	10	Hs_FMNL2_6
FNL2 siRNA_2	10	Hs_FMNL2_7
FNL2 siRNA_3	10	Hs_FMNL2_8
FNL3 siRNA_1	10	Hs_FMNL3_1
FNL3 siRNA_2	10	Hs_FMNL3_5
FNL3 siRNA_3	10	Hs_FMNL3_6
GFP siRNA	10	SI04380467
JMY siRNA_1	50	Hs_JMY_1
JMY siRNA_2	50	Hs_JMY_5
DIAPH2 siRNA_1	10	Hs_DIAPH2_1

DIAPH2 siRNA_2	10	Hs_DIAPH2_4
DIAPH2 siRNA_3	10	Hs_DIAPH2_6
N-WASP siRNA_1	10	Hs_WASL_1
N-WASP siRNA_2	10	Hs_WASL_6
SNX2 siRNA_1	10	Hs_SNX2_1
SNX2 siRNA_2	10	Hs_SNX2_3
WASH siRNA_1	20	Hs_WASH1_4
WASH siRNA_2	20	Hs_WASH1_8
WAVE1 siRNA_1	20	Hs_WASF1_3
WAVE1 siRNA_2	50	Hs_WASF1_4
WAVE2 siRNA_1	10	Hs_WASF2_5
WAVE2 siRNA_2	10	Hs_WASF2_6
WHAMM siRNA_1	50	Hs_WHDC1_1
WHAMM siRNA_2	50	Hs_WHDC1_2
Vps26 siRNA_1	10	Hs_VPS26A_1
Vps26 siRNA_2	10	Hs_VPS26A_2
Vps29 siRNA_1	10	Hs_VPS29_6
Vps29 siRNA_2	10	Hs_VPS29_2

References

Aksoy, P., Gottschalk, E. Y. and Meneses, P. I. (2017) ‘HPV entry into cells’, *Mutation Research - Reviews in Mutation Research*. Elsevier B.V., 772, pp. 13–22. doi: 10.1016/j.mrrev.2016.09.004.

Aydin, I. *et al.* (2014) ‘Large scale RNAi reveals the requirement of nuclear envelope breakdown for nuclear import of human papillomaviruses.’, *PLoS pathogens*, 10(5), p. e1004162. doi: 10.1371/journal.ppat.1004162.

Bannach, C. *et al.* (2020) ‘Epidermal growth factor receptor and Abl2 kinase regulate distinct steps of Human papillomavirus type 16 endocytosis.’, *Journal of virology*, 2(March). doi: 10.1128/JVI.02143-19.

Becker, M. *et al.* (2018) ‘Extracellular conformational changes in the capsid of human papillomaviruses contribute to asynchronous uptake into host cells’, *Journal of Virology*, 92(11), p. JVI.02106-17. doi: 10.1128/jvi.02106-17.

Bement, W. M., Sokac, A. M. and Mandato, C. A. (2003) ‘Four-dimensional imaging of cytoskeletal dynamics in Xenopus oocytes and eggs’, *Differentiation*, 71(9–10), pp. 518–527. doi: 10.1111/j.1432-0436.2003.07109005.x.

Bienkowska-Haba, M. *et al.* (2012) ‘Cyclophilins facilitate dissociation of the human papillomavirus type 16 capsid protein L1 from the L2/DNA complex following virus entry.’, *Journal of virology*, 86(18), pp. 9875–87. doi: 10.1128/JVI.00980-12.

Borradori, L. and Sonnenberg, A. (1999) ‘Structure and function of hemidesmosomes: More than simple adhesion complexes’, *Journal of Investigative Dermatology*, 112(4), pp. 411–418. doi: 10.1046/j.1523-1747.1999.00546.x.

Boukamp, P. *et al.* (1988) ‘Normal keratinization in a spontaneously immortalized aneuploid human keratinocyte cell line.’, *The Journal of cell biology*, 106(3), pp. 761–71. doi: 10.1083/jcb.106.3.761.

Brockman, W. W. and Nathans, D. (1974) ‘The isolation of simian virus 40 variants with specifically altered genomes’, *Proceedings of the National Academy of Sciences of the United States of America*, 71(3), pp. 942–946. doi: 10.1073/pnas.71.3.942.

Bucher, D. *et al.* (2018) ‘Clathrin-Adaptor ratio and membrane tension regulate the flat-To-curved transition of the clathrin coat during endocytosis’, *Nature Communications*, 9(1), pp. 1–13. doi: 10.1038/s41467-018-03533-0.

Buck, C. B. *et al.* (2005) ‘Generation of HPV pseudovirions using transfection and their use in neutralization assays.’, *Methods in molecular medicine*, 119, pp. 445–62. doi: 10.1385/1-59259-982-6:445.

Buck, C. B. and Thompson, C. D. (2007) ‘Production of Papillomavirus-Based Gene Transfer Vectors’, *Current Protocols in Cell Biology*, 37(1), pp. 26.1.1-26.1.19. doi: 10.1002/0471143030.cb2601s37.

Bujny, M. V *et al.* (2007) ‘The retromer component sorting nexin-1 is required for efficient retrograde transport of Shiga toxin from early endosome to the trans Golgi network.’, *Journal of cell science*, 120, pp. 2010–2021. doi: 10.1242/jcs.003111.

Campellone, K. G. *et al.* (2008) ‘WHAMM Is an Arp2/3 Complex Activator That Binds Microtubules and Functions in ER to Golgi Transport’, *Cell*, 134(1), pp. 148–161. doi: 10.1016/j.cell.2008.05.032.

Cao, H., Garcia, F. and Mcniven, M. A. (1998) ‘Differential Distribution of Dynamin Isoforms in Mammalian Cells’, *Molecular Biology of the Cell*, 9(September), pp. 2595–2609. doi: 10.1091/mbc.9.9.2595.

Carlton, J. G. *et al.* (2005) ‘Sorting nexin-2 is associated with tubular elements of the early endosome, but is not essential for retromer-mediated endosome-to-TGN transport.’, *Journal of cell science*, 118(Pt 19), pp. 4527–39. doi: 10.1242/jcs.02568.

Cerqueira, C. *et al.* (2013) ‘Heparin increases the infectivity of Human Papillomavirus Type 16 independent of cell surface proteoglycans and induces L1 epitope exposure’, *Cellular Microbiology*, 15(11), pp. 1818–1836. doi: 10.1111/cmi.12150.

Cerqueira, C. *et al.* (2015) ‘Kallikrein-8 Proteolytically Processes Human Papillomaviruses in the Extracellular Space To Facilitate Entry into Host Cells.’, *Journal of virology*, 89(14), pp. 7038–52. doi: 10.1128/JVI.00234-15.

Chadda, R. *et al.* (2007) ‘Cholesterol-sensitive Cdc42 activation regulates actin polymerization for endocytosis via the GEEC pathway’, *Traffic*, 8(6), pp. 702–717. doi: 10.1111/j.1600-0854.2007.00565.x.

Collins, A. *et al.* (2011) ‘Structural organization of the actin cytoskeleton at sites of clathrin-mediated endocytosis’, *Current Biology*, 21(14), pp. 1167–1175. doi: 10.1016/j.cub.2011.05.048.

Culp, T. D. *et al.* (2006) ‘Keratinocyte-Secreted Laminin 5 Can Function as a Transient Receptor for Human Papillomaviruses by Binding Virions and Transferring Them to Adjacent Cells’, *Journal of Virology*, 80(18), pp. 8940–8950. doi: 10.1128/jvi.00724-06.

Cureton, D. K. *et al.* (2009) ‘Vesicular Stomatitis Virus Enters Cells through Vesicles Incompletely Coated with Clathrin That Depend upon Actin for Internalization’, *PLoS Pathogens*, 5(4). doi: 10.1371/journal.ppat.1000394.

Dawson, J. C., Legg, J. A. and Machesky, L. M. (2006) ‘Bar domain proteins: a role in tubulation, scission and actin assembly in clathrin-mediated endocytosis’, *Trends in Cell Biology*, 16(10), pp. 493–498. doi: 10.1016/j.tcb.2006.08.004.

Day, P. M. *et al.* (2013) ‘Identification of a role for the trans-Golgi network in human papillomavirus 16 pseudovirus infection.’, *Journal of virology*, 87(7), pp. 3862–70. doi: 10.1128/JVI.03222-12.

Day, P. M., Lowy, D. R. and Schiller, J. T. (2003) ‘Papillomaviruses infect cells via a clathrin-dependent pathway’, *Virology*, 307(1), pp. 1–11. doi: 10.1016/S0042-6822(02)00143-5.

Derivery, E. *et al.* (2009) ‘The Arp2/3 Activator WASH Controls the Fission of Endosomes through a Large Multiprotein Complex’, *Developmental Cell*, 17(5), pp. 712–723. doi: 10.1016/j.devcel.2009.09.010.

DeTulleo, L. and Kirchhausen, T. (1998) ‘The clathrin endocytic pathway in viral infection’, *EMBO Journal*, 17(16), pp. 4585–4593. doi: 10.1093/emboj/17.16.4585.

Doherty, G. J. and McMahon, H. T. (2009) ‘Mechanisms of endocytosis.’, *Annual review of biochemistry*, 78(April), pp. 857–902. doi: 10.1146/annurev.biochem.78.081307.110540.

Doorbar, J. (2005) ‘The papillomavirus life cycle.’, *Journal of clinical virology□: the official publication of the Pan American Society for Clinical Virology*, 32 Suppl 1(SUPPL.), pp. S7-15. doi: 10.1016/j.jcv.2004.12.006.

Duleh, S. N. and Welch, M. D. (2010) ‘WASH and the Arp2/3 complex regulate endosome shape and trafficking’, *Cytoskeleton*, 67(3), p. NA-NA. doi: 10.1002/cm.20437.

Dziduszko, A. and Ozbun, M. A. (2013) ‘Annexin A2 and S100A10 regulate human papillomavirus type 16 entry and intracellular trafficking in human keratinocytes.’, *Journal of virology*, 87(13), pp. 7502–15. doi: 10.1128/JVI.00519-13.

Engel, S. *et al.* (2011) ‘Role of endosomes in simian virus 40 entry and infection.’, *Journal of virology*, 85(9), pp. 4198–4211. doi: 10.1128/JVI.02179-10.

Evander, M. *et al.* (1997) ‘Identification of the alpha6 integrin as a candidate receptor for papillomaviruses.’, *Journal of virology*, 71(3), pp. 2449–56. Available at: http://www.ncbi.nlm.nih.gov/pubmed/9032382%5Cnhttp://www.pubmedcentral.nih.gov/articlerender.fcgi?artid=PMC191355.

Ezratty, E. J., Partridge, M. A. and Gundersen, G. G. (2005) ‘Microtubule-induced focal adhesion disassembly is mediated by dynamin and focal adhesion kinase’, *Nature Cell Biology*, 7(6), pp. 581–590. doi: 10.1038/ncb1262.

Fast, L. A. *et al.* (2018) ‘Inhibition of tetraspanin functions impairs human papillomavirus and cytomegalovirus infections’, *International Journal of Molecular Sciences*, 19(10). doi: 10.3390/ijms19103007.

Florin, L. and Lang, T. (2018) ‘Tetraspanin Assemblies in Virus Infection’, *Frontiers in Immunology*, 9(May), pp. 1–9. doi: 10.3389/fimmu.2018.01140.

Gallop, J. L. *et al.* (2006) ‘Mechanism of endophilin N-BAR domain-mediated membrane curvature.’, *The EMBO journal*, 25(12), pp. 2898–2910. doi: 10.1038/sj.emboj.7601174.

Giroglou, T. *et al.* (2001) ‘Human Papillomavirus Infection Requires Cell Surface Heparan Sulfate’, *Journal of Virology*, 75(3), pp. 1565–1570. doi: 10.1128/JVI.75.3.1565.

Gomez, T. S. and Billadeau, D. D. (2009) ‘A FAM21-Containing WASH Complex Regulates Retromer-Dependent Sorting’, *Developmental Cell*, 17(5), pp. 699–711. doi: 10.1016/j.devcel.2009.09.009.

Hafezi, W. *et al.* (2012) ‘Entry of herpes simplex virus type 1 (HSV-1) into the distal axons of trigeminal neurons favors the onset of nonproductive, silent infection’, *PLoS Pathogens*, 8(5). doi: 10.1371/journal.ppat.1002679.

Hänisch, J. *et al.* (2010) ‘Molecular dissection of Salmonella-induced membrane ruffling versus invasion’, *Cellular Microbiology*, 12(1), pp. 84–98. doi: 10.1111/j.1462-5822.2009.01380.x.

Hao, Y. *et al.* (2013) ‘Regulation of WASH-Dependent Actin Polymerization and Protein Trafficking by Ubiquitination’, *Cell*, 152(5), pp. 1051–1064. doi: 10.1016/j.cell.2013.01.051.

Harbour, M. E., Breusegem, S. Y. and Seaman, M. N. J. (2012) ‘Recruitment of the endosomal WASH complex is mediated by the extended “tail” of Fam21 binding to the retromer protein Vps35’, *Biochemical Journal*, 442(1), pp. 209–220. doi: 10.1042/BJ20111761.

Hayer, A. *et al.* (2010) ‘Biogenesis of caveolae: Stepwise assembly of large caveolin and cavin complexes’, *Traffic*, 11(3), pp. 361–382. doi: 10.1111/j.1600-0854.2009.01023.x.

Helenius, A. (2018) ‘Virus Entry: Looking Back and Moving Forward’, *Journal of Molecular Biology*. Elsevier Ltd, 430(13), pp. 1853–1862. doi: 10.1016/j.jmb.2018.03.034.

Helenius, A. (2020) ‘Standing on the Shoulders of Viruses’, *Annual Review of Biochemistry*, 89, pp. 21–43. doi: 10.1146/annurev-biochem-011320-103928.

Helfer, E. *et al.* (2013) ‘Endosomal recruitment of the WASH complex: Active sequences and mutations impairing interaction with the retromer’, *Biology of the Cell*, 105(5), pp. 191–207. doi: 10.1111/boc.201200038.

Heuser, J. and Evans, L. (1980) ‘Three-dimensional visualization of coated vesicle formation in fibroblasts’, *Journal of Cell Biology*, 84(3), pp. 560–583. doi: 10.1083/jcb.84.3.560.

Hinshaw, J. E. and Schmid, S. L. (1995) ‘Dynamin self-assembles into rings suggesting a mechanism for coated vesicle budding.’, *Nature*, 374(6518), pp. 190–2. doi: 10.1038/374190a0.

Huang, C.-Y. *et al.* (2008) ‘A novel cellular protein, VPEF, facilitates vaccinia virus penetration into HeLa cells through fluid phase endocytosis.’, *Journal of virology*, 82(16), pp. 7988–99. doi: 10.1128/JVI.00894-08.

Humbel, B. M., Stierhof, Y.-D. (2009) ‘Cryosectioning according to Tokuyasu’, in Cavalier, A., Spehner, D., Humbel, B. M. (ed.) *Handbook of cryopreparation methods for electron microscopy*.

Hwang, S., Takimoto, T. and Hemler, M. E. (2019) ‘Integrin-independent support of cancer drug resistance by tetraspanin CD151’, *Cellular and Molecular Life Sciences*. Springer International Publishing, 76(8), pp. 1595–1604. doi: 10.1007/s00018-019-03014-7.

Jao, C. C. *et al.* (2010) ‘Roles of amphipathic helices and the bin/amphiphysin/rvs (BAR) domain of endophilin in membrane curvature generation’, *Journal of Biological Chemistry*, 285(26), pp. 20164–20170. doi: 10.1074/jbc.M110.127811.

Jia, D. *et al.* (2012) ‘Multiple repeat elements within the FAM21 tail link the WASH actin regulatory complex to the retromer’, *Molecular Biology of the Cell*, 23, pp. 2352–2361. doi: 10.1091/mbc.E11-12-1059.

Johannsdottir, H. K. *et al.* (2009) ‘Host cell factors and functions involved in vesicular stomatitis virus entry.’, *Journal of virology*, 83(1), pp. 440–53. doi: 10.1128/JVI.01864-08.

Johnson, K. M. *et al.* (2009) ‘Role of Heparan Sulfate in Attachment to and Infection of the Murine Female Genital Tract by Human Papillomavirus’, *Journal of Virology*, 83(5), pp. 2067–2074. doi: 10.1128/jvi.02190-08.

Jones, J. C. R., Hopkinson, S. B. and Goldfinger, L. E. (1998) ‘Structure and assembly of hemidesmosomes’, *BioEssays*, 20(6), pp. 488–494. doi: 10.1002/(SICI)1521-1878(199806)20:6<488::AID-BIES7>3.0.CO;2-I.

Kage, F. *et al.* (2017) ‘FMNL formins boost lamellipodial force generation’, *Nature Communications*, 8. doi: 10.1038/ncomms14832.

Kaksonen, M. and Roux, A. (2018) ‘Mechanisms of clathrin-mediated endocytosis’, *Nature Reviews Molecular Cell Biology*. Nature Publishing Group, 19(5), pp. 313–326. doi: 10.1038/nrm.2017.132.

Kamentsky, L. *et al.* (2011) ‘Improved structure, function and compatibility for cellprofiler: Modular high-throughput image analysis software’, *Bioinformatics*, 27(8), pp. 1179–1180. doi: 10.1093/bioinformatics/btr095.

Kirkham, M. *et al.* (2005) ‘Ultrastructural identification of uncoated caveolin-independent early endocytic vehicles’, *Journal of Cell Biology*, 168(3), pp. 465–476. doi: 10.1083/jcb.200407078.

Kvainickas, A. *et al.* (2017) ‘Cargo-selective SNX-BAR proteins mediate retromer trimer independent retrograde transport.’, *The Journal of cell biology*, p. jcb.201702137. doi: 10.1083/jcb.201702137.

Lakshminarayan, R. *et al.* (2014) ‘Galectin-3 drives glycosphingolipid-dependent biogenesis of clathrin-independent carriers’, *Nature Cell Biology*, 16(6), pp. 592–603. doi: 10.1038/ncb2970.

Landry, J. J. M. *et al.* (2013) ‘The genomic and transcriptomic landscape of a HeLa cell line.’, *G3 (Bethesda, Md.)*, 3(8), pp. 1213–24. doi: 10.1534/g3.113.005777.

Liberali, P. *et al.* (2008) ‘The closure of Pak1-dependent macropinosomes requires the phosphorylation of CtBP1/BARS.’, *The EMBO journal*, 27(7), pp. 970–81. doi: 10.1038/emboj.2008.59.

Lim, J. P. and Gleeson, P. A. (2011) ‘Macropinocytosis: an endocytic pathway for internalising large gulps’, *Immunology and Cell Biology*, 89(8), pp. 836–843. doi: 10.1038/icb.2011.20.

Linardopoulou, E. V *et al.* (2007) ‘Human subtelomeric WASH genes encode a new subclass of the WASP family.’, *PLoS genetics*, 3(12), p. e237. doi: 10.1371/journal.pgen.0030237.

Lipovsky, A. *et al.* (2013) ‘Genome-wide siRNA screen identifies the retromer as a cellular entry factor for human papillomavirus.’, *Proceedings of the National Academy of Sciences of the United States of America*, 110(18), pp. 7452–7. doi: 10.1073/pnas.1302164110.

Lipovsky, A. *et al.* (2015) ‘Application of the proximity-dependent assay and fluorescence imaging approaches to study viral entry pathways.’, *Methods in molecular biology (Clifton, N.J.)*, 1270, pp. 437–51. doi: 10.1007/978-1-4939-2309-0_30.

Liu, L. *et al.* (2007) ‘Tetraspanin CD151 promotes cell migration by regulating integrin trafficking’, *Journal of Biological Chemistry*, 282(43), pp. 31631–31642. doi: 10.1074/jbc.M701165200.

Loerke, D. *et al.* (2009) ‘Cargo and Dynamin Regulate Clathrin-Coated Pit Maturation’, *PLoS Biology*, 7(3). doi: 10.1371/journal.pbio.1000057.

Machesky, L. M. and Insall, R. H. (1998) ‘Scar1 and the related Wiskott-Aldrich syndrome protein, WASP, regulate the actin cytoskeleton through the Arp2/3 complex’, *Current Biology*, 8(25), pp. 1347–1356. doi: 10.1016/S0960-9822(98)00015-3.

Marsh, M. and Helenius, A. (1980) ‘Adsorptive endocytosis of Semliki Forest virus’, *Journal of Molecular Biology*, 142(3), pp. 439–454. doi: 10.1016/0022-2836(80)90281-8.

Marsh, M. and Helenius, A. (2006) ‘Virus entry: Open sesame’, *Cell*, 124(4), pp. 729–740. doi: 10.1016/j.cell.2006.02.007.

Marsh, M., Kielian, M. C. and Helenius, A. (1984) ‘Semliki forest virus entry and the endocytic pathway’, *Biochemical Society Transactions*, 12(6), pp. 981–983. doi: 10.1042/bst0120981.

Mazzon, M. and Mercer, J. (2014) ‘Lipid Interactions During Virus Entry and Infection’, *Cellular Microbiology*, 16(September), p. n/a-n/a. doi: 10.1111/cmi.12340.

McMahon, H. T. and Boucrot, E. (2011) ‘Molecular mechanism and physiological functions of clathrin-mediated endocytosis’, *Nature Publishing Group*, 12(8), pp. 517–533. doi: 10.1038/nrm3151.

Ménager, M. M. and Littman, D. R. (2016) ‘Actin Dynamics Regulates Dendritic Cell-Mediated Transfer of HIV-1 to T Cells’, *Cell*, 164(4), pp. 695–709. doi: 10.1016/j.cell.2015.12.036.

Mercer, J. and Helenius, A. (2008) ‘Vaccinia virus uses macropinocytosis and apoptotic mimicry to enter host cells.’, *Science (New York, N.Y.)*, 320(5875), pp. 531–535. doi: 10.1126/science.1155164.

Mercer, J., Schelhaas, M. and Helenius, A. (2010) ‘Virus entry by endocytosis.’, *Annual review of biochemistry*, 79, pp. 803–33. doi: 10.1146/annurev-biochem-

060208-104626.

Merrifield, C. J. *et al.* (2002) ‘Imaging actin and dynamin recruitment during invagination of single clathrin-coated pits’, *Nat Cell Biol*, 4(9), pp. 691–698. doi: 10.1038/ncb837.

Merrifield, C. J. (2004) ‘Seeing is believing: Imaging actin dynamics at single sites of endocytosis’, *Trends in Cell Biology*, 14(7), pp. 352–358. doi: 10.1016/j.tcb.2004.05.008.

Merrifield, C. J. and Kaksonen, M. (2014) ‘Endocytic accessory factors and regulation of clathrin-mediated endocytosis.’, *Cold Spring Harbor perspectives in biology*, 6(11), p. a016733. doi: 10.1101/cshperspect.a016733.

Mikuličić, S. *et al.* (2019) ‘ADAM17-dependent signaling is required for oncogenic human papillomavirus entry platform assembly.’, *eLife*, 8. doi: 10.7554/eLife.44345.

Mirabello, L. *et al.* (2017) ‘HPV16 E7 Genetic Conservation Is Critical to Carcinogenesis’, *Cell*, 170(6), pp. 1164-1174.e6. doi: 10.1016/j.cell.2017.08.001.

Mooren, O. L., Galletta, B. J. and Cooper, J. A. (2012) ‘Roles for Actin Assembly in Endocytosis’, *Annu. Rev. Biochem*, 81(May), pp. 661–86. doi: 10.1146/annurev-biochem-060910-094416.

Morlot, S. and Roux, A. (2013) ‘Mechanics of dynamin-mediated membrane fission.’, *Annual review of biophysics*, 42, pp. 629–49. doi: 10.1146/annurev-biophys-050511-102247.

Nicola, A. V. *et al.* (2005) ‘Herpes Simplex Virus Type 1 Enters Human Epidermal Keratinocytes, but Not Neurons, via a pH-Dependent Endocytic Pathway’, *Journal of Virology*, 79(12), pp. 7609–7616. doi: 10.1128/jvi.79.12.7609-7616.2005.

Owaribe, K. *et al.* (1990) ‘The hemidesmosomal plaque’, *Differentiation*, 45(3), pp. 207–220. doi: 10.1111/j.1432-0436.1990.tb00475.x.

Pelkmans, L. *et al.* (2004) ‘Caveolin-stabilized membrane domains as multifunctional transport and sorting devices in endocytic membrane traffic’, *Cell*, 118(6), pp. 767–780. doi: 10.1016/j.cell.2004.09.003.

Pelkmans, L., Püntener, D. and Helenius (2002) ‘Local Actin Polymerization and Dynamin Recruitment in SV40-Induced Internalization of Caveolae’, *Science*, 296(5567), pp. 535–539. doi: 10.1126/science.1069784.

Popa, A. *et al.* (2015) ‘Direct Binding of Retromer to Human Papillomavirus Type 16 Minor Capsid Protein L2 Mediates Endosome Exit during Viral Infection’, *PLoS Pathogens*, 11(2), pp. 1–21. doi: 10.1371/journal.ppat.1004699.

Popoff, V. *et al.* (2007) ‘The retromer complex and clathrin define an early endosomal retrograde exit site’, *Journal of Cell Science*, 120(12), pp. 2022–2031. doi: 10.1242/jcs.003020.

Pyeon, D. *et al.* (2009) ‘Establishment of human papillomavirus infection requires cell cycle progression’, *PLoS Pathogens*, 5(2). doi: 10.1371/journal.ppat.1000318.

Qualmann, B. and Kelly, R. B. (2000) ‘Syndapin isoforms participate in receptor-mediated endocytosis and actin organization’, *Journal of Cell Biology*, 148(5), pp. 1047–1061. doi: 10.1083/jcb.148.5.1047.

Qualmann, B., Koch, D. and Kessels, M. M. (2011) ‘Let’s go bananas: revisiting the endocytic BAR code.’, *The EMBO journal*, 30(17), pp. 3501–15. doi: 10.1038/emboj.2011.266.

Quirin, K. *et al.* (2008) ‘Lymphocytic choriomeningitis virus uses a novel endocytic pathway for infectious entry via late endosomes’, *Virology*, 378(1), pp. 21–33. doi: 10.1016/j.virol.2008.04.046.

Raff, A. B. *et al.* (2013) ‘The Evolving Field of Human Papillomavirus Receptor Research: a Review of Binding and Entry’, *Journal of Virology*, 87(11), pp. 6062–6072. doi: 10.1128/JVI.00330-13.

Ran, F. A. *et al.* (2013) ‘Genome engineering using the CRISPR-Cas9 system.’, *Nat Protoc*, 8(11), pp. 2281–2308. doi: 10.1038/nprot.2013.143.

Richards, R. M. *et al.* (2006) ‘Cleavage of the papillomavirus minor capsid protein, L2, at a furin consensus site is necessary for infection.’, *Proceedings of the National Academy of Sciences of the United States of America*, 103(5), pp. 1522–7. doi: 10.1073/pnas.0508815103.

Riedl, J. *et al.* (2008) ‘Lifeact: a versatile marker to visualize F-actin.’, *Nature methods*, 5(7), pp. 605–7. doi: 10.1038/nmeth.1220.

Rizvi, S. A. *et al.* (2009) ‘Identification and Characterization of a Small Molecule Inhibitor of Formin-Mediated Actin Assembly’, *Chemistry and Biology*. Elsevier Ltd, 16(11), pp. 1158–1168. doi: 10.1016/j.chembiol.2009.10.006.

Roberts, J. N. *et al.* (2007) ‘Genital transmission of HPV in a mouse model is potentiated by nonoxynol-9 and inhibited by carrageenan’, *Nature Medicine*, 13(7), pp. 857–861. doi: 10.1038/nm1598.

Rojek, J. M., Perez, M. and Kunz, S. (2008) ‘Cellular Entry of Lymphocytic Choriomeningitis Virus’, *Journal of Virology*, 82(3), pp. 1505–1517. doi: 10.1128/jvi.01331-07.

Rottner, K., Hänisch, J. and Campellone, K. G. (2010) ‘WASH, WHAMM and JMY: regulation of Arp2/3 complex and beyond.’, *Trends in cell biology*, 20(11), pp. 650–61. doi: 10.1016/j.tcb.2010.08.014.

Rust, M. J. *et al.* (2004) ‘Assembly of endocytic machinery around individual influenza viruses during viral entry’, *Nature Structural and Molecular Biology*, 11(6), pp. 567–573. doi: 10.1038/nsmb769.

Saalfeld, S. and Tomancák, P. (2008) ‘Automatic landmark correspondence detection for ImageJ’, *Proceedings of the ImageJ User and Developer Conference*, pp. 128–133. Available at: http://fly.mpi-cbg.de/~saalfeld/Publications/download/imagejconf2008.pdf.

de Sanjose, S. *et al.* (2010) ‘Human papillomavirus genotype attribution in invasive cervical cancer: a retrospective cross-sectional worldwide study’, *The Lancet Oncology*, 11(11), pp. 1048–1056. doi: 10.1016/S1470-2045(10)70230-8.

Scheffer, K. D. *et al.* (2013) ‘Tetraspanin CD151 Mediates Papillomavirus Type 16 Endocytosis’, *Journal of Virology*, 87(6), pp. 3435–3446. doi: 10.1128/JVI.02906-12.

Schelhaas, M. *et al.* (2003) ‘Herpes simplex virus type 1 exhibits a tropism for basal entry in polarized epithelial cells’, *Journal of General Virology*, 84(9), pp. 2473–2484. doi: 10.1099/vir.0.19226-0.

Schelhaas, M. *et al.* (2008) ‘Human papillomavirus type 16 entry: Retrograde cell surface transport along actin-rich protrusions’, *PLoS Pathogens*, 4(9). doi: 10.1371/journal.ppat.1000148.

Schelhaas, M. *et al.* (2012) ‘Entry of human papillomavirus type 16 by actin-dependent, clathrin- and lipid raft-independent endocytosis.’, *PLoS pathogens*, 8(4), p. e1002657. doi: 10.1371/journal.ppat.1002657.

Schindelin, J. *et al.* (2012) ‘Fiji: An open-source platform for biological-image analysis’, *Nature Methods*, 9(7), pp. 676–682. doi: 10.1038/nmeth.2019.

Schmid, S. L. and Conner, S. D. (2003) ‘Regulated portals of entry into the cell’, *Nature*, 422(March), pp. 37–44. Available at: www.nature.com/nature.

Seaman, M. N. J. (2012) ‘The retromer complex - endosomal protein recycling and beyond.’, *Journal of cell science*, 125(Pt 20), pp. 4693–702. doi: 10.1242/jcs.103440.

Selinka, H.-C. *et al.* (2007) ‘Inhibition of transfer to secondary receptors by heparan sulfate-binding drug or antibody induces noninfectious uptake of human papillomavirus.’, *Journal of virology*, 81(20), pp. 10970–80. doi: 10.1128/JVI.00998-07.

Shikama, N. *et al.* (1999) ‘A novel cofactor for p300 that regulates the p53 response’, *Molecular Cell*, 4(3), pp. 365–376. doi: 10.1016/S1097-2765(00)80338-X.

Shin, N. *et al.* (2008) ‘SNX9 regulates tubular invagination of the plasma membrane through interaction with actiAn cytoskeleton and dynamin 2.’, *Journal of cell science*, 121(Pt 8), pp. 1252–63. doi: 10.1242/jcs.016709.

Siddiqa, A. *et al.* (2018) ‘Human Papillomavirus 16 Infection Induces VAP-Dependent Endosomal Tubulation’, *Journal of Virology*. Edited by R. M. Longnecker, 92(6), pp. 1–14. doi: 10.1128/JVI.01514-17.

Sieczkarski, S. B. and Whittaker, G. R. (2002) ‘Influenza virus can enter and infect cells in the absence of clathrin-mediated endocytosis.’, *Journal of virology*, 76(20), pp. 10455–64. doi: 10.1128/jvi.76.20.10455-10464.2002.

Simonetti, B. *et al.* (2017) ‘Sequence-dependent cargo recognition by SNX-BARs mediates retromer-independent transport of CI-MPR’, *Journal of Cell Biology*, 216(11), pp. 3695–3712. doi: 10.1083/jcb.201703015.

Singh, I. and Helenius, A. (1992) ‘Role of ribosomes in Semliki Forest virus nucleocapsid uncoating.’, *Journal of Virology*, 66(12), pp. 7049–7058. doi: 10.1128/jvi.66.12.7049-7058.1992.

Smith, J. L. *et al.* (2008) ‘Caveolin-1-Dependent Infectious Entry of Human Papillomavirus Type 31 in Human Keratinocytes Proceeds to the Endosomal Pathway for pH-Dependent Uncoating’, *Journal of Virology*, 82(19), pp. 9505–9512. doi: 10.1128/jvi.01014-08.

Snijder, B. *et al.* (2012) ‘Single-cell analysis of population context advances RNAi screening at multiple levels.’, *Molecular systems biology*, 8(579), p. 579. doi: 10.1038/msb.2012.9.

Sochacki, K. A. *et al.* (2014) ‘Correlative super-resolution fluorescence and metal-replica transmission electron microscopy’, *Nature Methods*, 11(3), pp. 305–308. doi: 10.1038/nmeth.2816.

Söderberg, O. *et al.* (2006) ‘Direct observation of individual endogenous protein complexes in situ by proximity ligation’, *Nature Methods*, 3(12), pp. 995–1000. doi: 10.1038/nmeth947.

Sokac, A. M. *et al.* (2003) ‘Cdc42-dependent actin polymerization during compensatory endocytosis in Xenopus eggs.’, *Nature cell biology*, 5(8), pp. 727–732. doi: 10.1038/ncb1025.

Soulet, F. *et al.* (2005) ‘SNX9 Regulates Dynamin Assembly and Is Required for

Efficient Clathrin-mediated Endocytosis', *Molecular Biology of the Cell*, 16(4), pp. 2058–2067. doi: 10.1091/mbc.e04-11-1016.

Spoden, G. *et al.* (2008) 'Clathrin- and caveolin-independent entry of human papillomavirus type 16--involvement of tetraspanin-enriched microdomains (TEMs).', *PloS one*, 3(10), p. e3313. doi: 10.1371/journal.pone.0003313.

Stechmann, B. *et al.* (2010) 'Inhibition of retrograde transport protects mice from lethal ricin challenge', *Cell*, 141(2), pp. 231–242. doi: 10.1016/j.cell.2010.01.043.

Steffen, A. *et al.* (2006) 'Filopodia Formation in the Absence of Functional WAVE- and Arp2/3-Complexes', *Molecular Biology of the Cell*. Edited by M. Ginsberg, 17(6), pp. 2581–2591. doi: 10.1091/mbc.e05-11-1088.

Stoeber, M. *et al.* (2016) 'Model for the architecture of caveolae based on a flexible, net-like assembly of Cavin1 and Caveolin discs', *Proceedings of the National Academy of Sciences of the United States of America*, 113(50), pp. E8069–E8078. doi: 10.1073/pnas.1616838113.

Stradal, T. E. and Scita, G. (2006) 'Protein complexes regulating Arp2/3-mediated actin assembly', *Current Opinion in Cell Biology*, 18(1), pp. 4–10. doi: 10.1016/j.ceb.2005.12.003.

Suetsugu, S. *et al.* (2003) 'Differential roles of WAVE1 and WAVE2 in dorsal and peripheral ruffle formation for fibroblast cell migration', *Developmental Cell*, 5(4), pp. 595–609. doi: 10.1016/S1534-5807(03)00297-1.

Surviladze, Z., Dziduszko, A. and Ozbun, M. A. (2012) 'Essential roles for soluble virion-associated heparan sulfonated proteoglycans and growth factors in human papillomavirus infections.', *PLoS pathogens*, 8(2), p. e1002519. doi: 10.1371/journal.ppat.1002519.

Sweitzer, S. M. and Hinshaw, J. E. (1998) 'Dynamin undergoes a GTP-dependent conformational change causing vesiculation', *Cell*, 93(6), pp. 1021–1029. doi: 10.1016/S0092-8674(00)81207-6.

Takei, K. *et al.* (1995) 'Tubular membrane invaginations coated by dynamin rings are induced by GTP-γS in nerve terminals', *Nature*, 374(6518), pp. 186–190. doi: 10.1038/374186a0.

Taylor, M. J., Lampe, M. and Merrifield, C. J. (2012) 'A feedback loop between dynamin and actin recruitment during clathrin-mediated endocytosis', *PLoS Biology*, 10(4). doi: 10.1371/journal.pbio.1001302.

Taylor, M. J., Perrais, D. and Merrifield, C. J. (2011) 'A high precision survey of the molecular dynamics of mammalian clathrin-mediated endocytosis', *PLoS Biology*, 9(3). doi: 10.1371/journal.pbio.1000604.

Tokuyasu, K. T. (1980) 'Immunochemistry on ultrathin frozen sections', *The Histochemical Journal*, 12(4), pp. 381–403. doi: 10.1007/BF01011956.

Tsarouhas, V. *et al.* (2019) 'WASH phosphorylation balances endosomal versus cortical actin network integrities during epithelial morphogenesis', *Nature Communications*. Springer US, 10(1). doi: 10.1038/s41467-019-10229-6.

Valente, C., Luini, A. and Corda, D. (2013) 'Components of the CtBP1/BARS-dependent fission machinery', *Histochemistry and Cell Biology*, 140(4), pp. 407–421. doi: 10.1007/s00418-013-1138-1.

Ventayol, P. S. and Schelhaas, M. (2015) 'Fluorescently labeled human papillomavirus pseudovirions for use in virus entry experiments', *Current Protocols in Microbiology*, 2015(May), pp. 14B.4.1-14B.4.22. doi: 10.1002/9780471729259.mc14b04s37.

de Vries, E. *et al.* (2011) 'Dissection of the influenza a virus endocytic routes reveals macropinocytosis as an alternative entry pathway', *PLoS Pathogens*, 7(3), p. e1001329. doi: 10.1371/journal.ppat.1001329.

Walko, G., Castañón, M. J. and Wiche, G. (2015) 'Molecular architecture and function of the hemidesmosome', *Cell and Tissue Research*, 360(3), pp. 529–544. doi: 10.1007/s00441-015-2216-6.

Webb, D. J., Parsons, J. T. and Horwitz, A. F. (2002) 'Adhesion assembly, disassembly and turnover in migrating cells - Over and over and over again', *Nature Cell Biology*, 4(4). doi: 10.1038/ncb0402-e97.

Woodham, A. W. *et al.* (2012) 'The S100A10 subunit of the annexin A2 heterotetramer facilitates L2-mediated human papillomavirus infection.', *PloS one*, 7(8), p. e43519. doi: 10.1371/journal.pone.0043519.

Xie, J. *et al.* (2020) 'TBC1D5-Catalyzed Cycling of Rab7 Is Required for Retromer-Mediated Human Papillomavirus Trafficking during Virus Entry', *Cell Reports*, 31(10). doi: 10.1016/j.celrep.2020.107750.

Yarar, D., Waterman-Storer, C. M. and Schmid, S. L. (2007) 'SNX9 Couples Actin Assembly to Phosphoinositide Signals and Is Required for Membrane Remodeling during Endocytosis', *Developmental Cell*, 13(1), pp. 43–56. doi: 10.1016/j.devcel.2007.04.014.

Yong, X. *et al.* (2020) 'Mechanism of cargo recognition by retromerlinked SNX-BAR proteins', *PLoS Biology*, 18(3), pp. 1–29. doi: 10.1371/journal.pbio.3000631.

Yoon, C.-S. *et al.* (2001) 'α6 Integrin Is the Main Receptor of Human Papillomavirus Type 16 VLP', *Biochemical and Biophysical Research Communications*, 283(3), pp. 668–673. doi: 10.1006/bbrc.2001.4838.

Zhang, P. *et al.* (2018) 'Cell-Penetrating Peptide Mediates Intracellular Membrane Passage of Human Papillomavirus L2 Protein to Trigger Retrograde Trafficking', *Cell*, 174(6), pp. 1465-1476.e13. doi: 10.1016/j.cell.2018.07.031.

Zhong, Q. *et al.* (2002) 'Endosomal localization and function of sorting nexin 1.', *Proceedings of the National Academy of Sciences of the United States of America*, 99(10), pp. 6767–6772. doi: 10.1073/pnas.092142699.

Zuchero, J. B. *et al.* (2009) 'p53-cofactor JMY is a multifunctional actin nucleation factor', *Nature Cell Biology*, 11(4), pp. 451–459. doi: 10.1038/ncb1852.


A
early stage
intermediate stage
late stage
HPV16 endocytosis
clathrin mediated endocytosis
B
HPV16 localization (% of particles)
50
40
30
20
10
0
DMSO
cytoD
actin network
early stage
intermediate stage
late stage
clathrin coated
tubular structure
C
100
50
0
***
***
***
infection (%)
1
10
50
cytoD (µg/ml)
D
ctrl.
cytoD

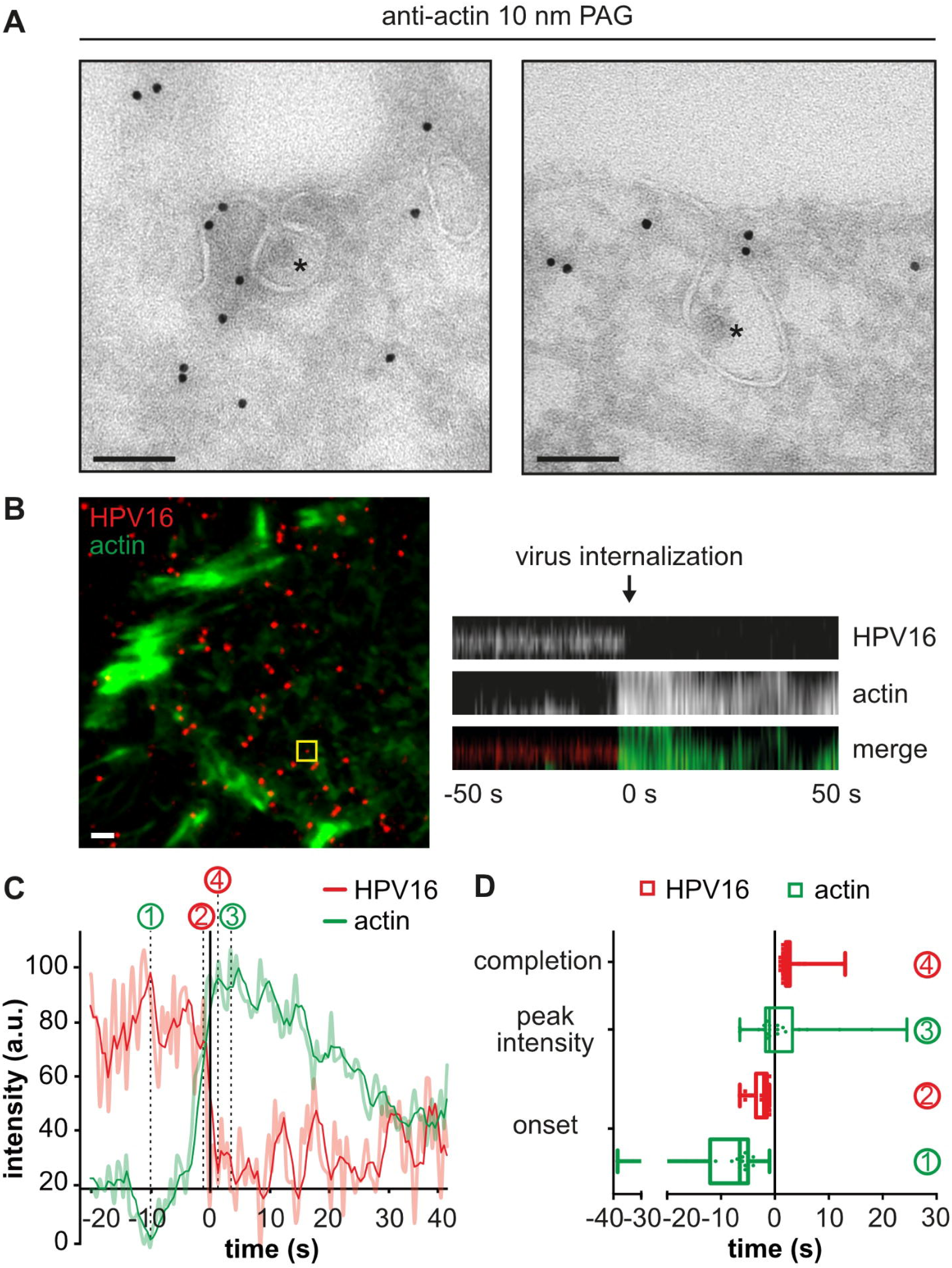
A
anti-actin 10 nm PAG
*
*
B
HPV16
actin
virus internalization
HPV16
actin
merge
-50 s
0 s
50 s
C
④
①
②
③
HPV16
actin
intensity (a.u.)
100
80
60
40
20
0
-20
-10
0
10
20
30
40
time (s)
D
HPV16
actin
completion
peak intensity
onset
④
③
②
①
-40
-30
-20
-10
0
10
20
30
time (s)

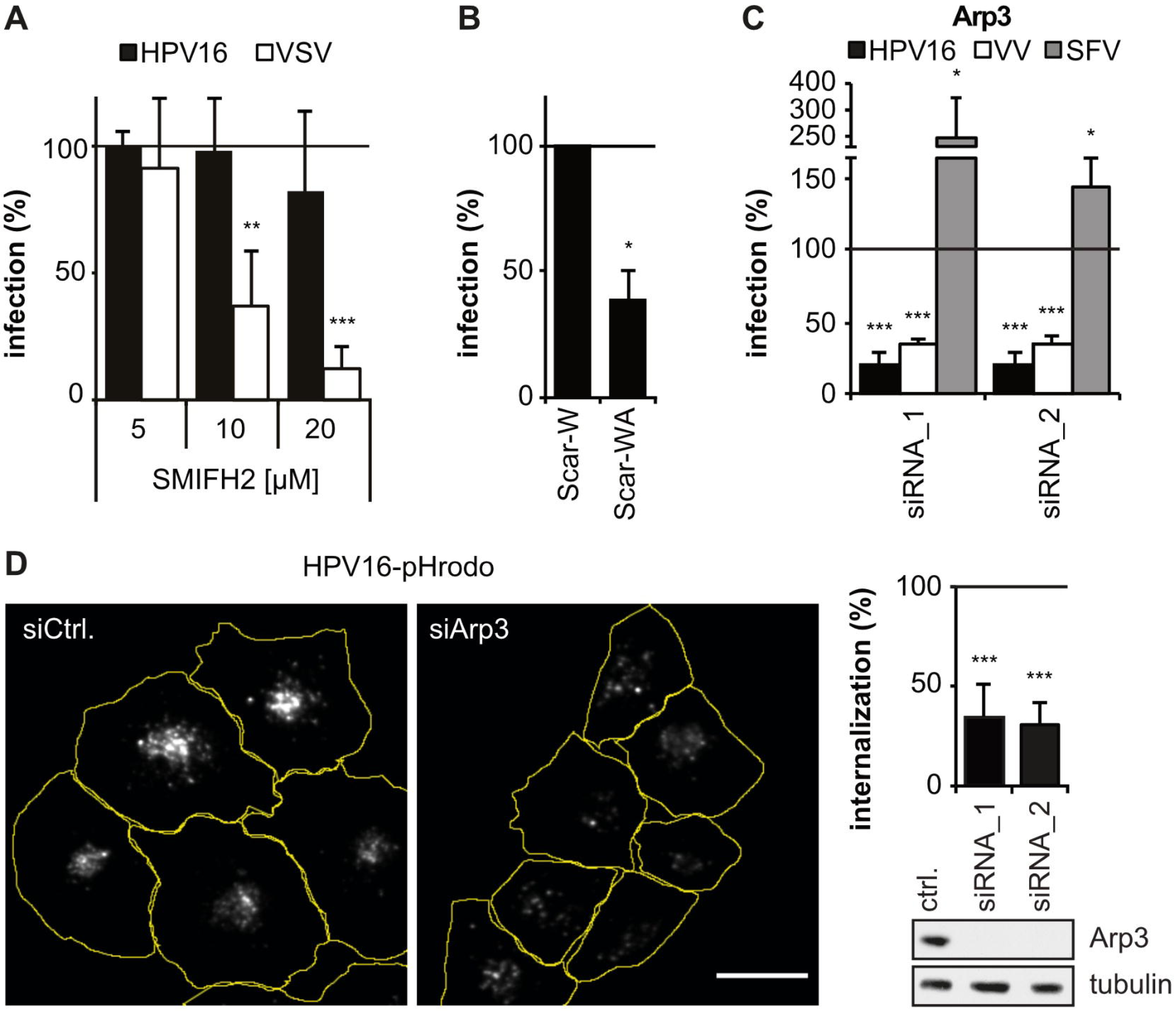
A
■HPV16 □VSV
infection (%)
100
50
0
**
***
5
10
20
SMIFH2 [µM]
B
infection (%)
100
50
0
*
Scar-W
Scar-WA
C
Arp3
■HPV16 □VV ■SFV
400
300
250
150
100
50
0
infection (%)
*
*
***
***
***
***
siRNA_1
siRNA_2
D
HPV16-pHrodo
siCtrl.
siArp3
internalization (%)
100
50
0
***
***
siRNA_1
siRNA_2
ctrl.
siRNA_1
siRNA_2
Arp3
tubulin

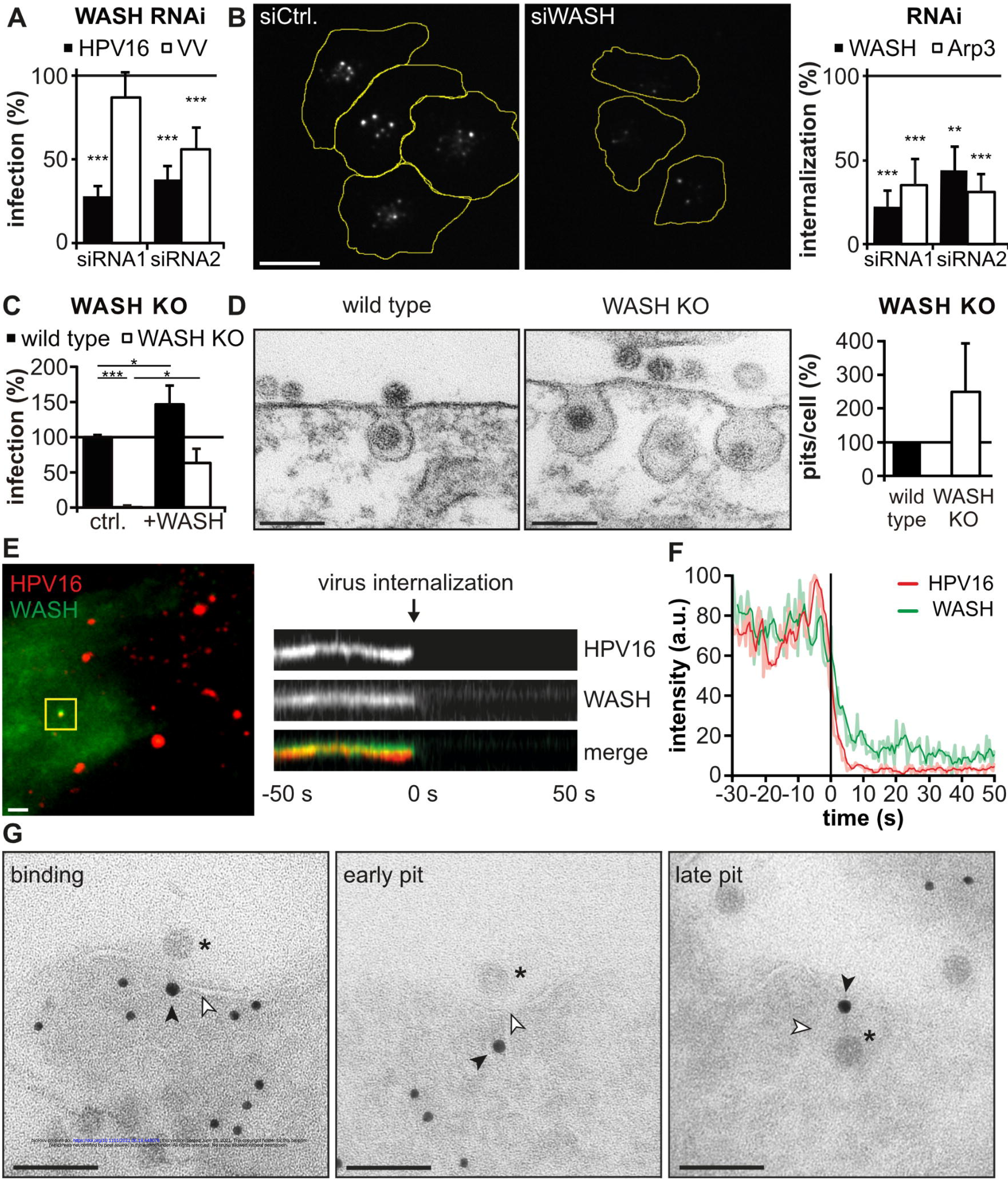
A
WASH RNAi
■ HPV16 □ VV
infection (%)
100
50
0
***
***
***
siRNA1
siRNA2
B
siCtrl.
siWASH
RNAi
■ WASH □ Arp3
internalization (%)
100
50
0
***
***
**
***
siRNA1
siRNA2
C
WASH KO
■ wild type □ WASH KO
infection (%)
200
150
100
50
0
*
***
*
ctrl.
+WASH
D
wild type
WASH KO
WASH KO
pits/cell (%)
400
300
200
100
0
wild type
WASH KO
E
HPV16
WASH
virus internalization
HPV16
WASH
merge
-50 s
0 s
50 s
F
HPV16
WASH
intensity (a.u.)
100
80
60
40
20
0
-30
-20
-10
0
10
20
30
40
50
time (s)
G
binding
early pit
late pit
*
*
*

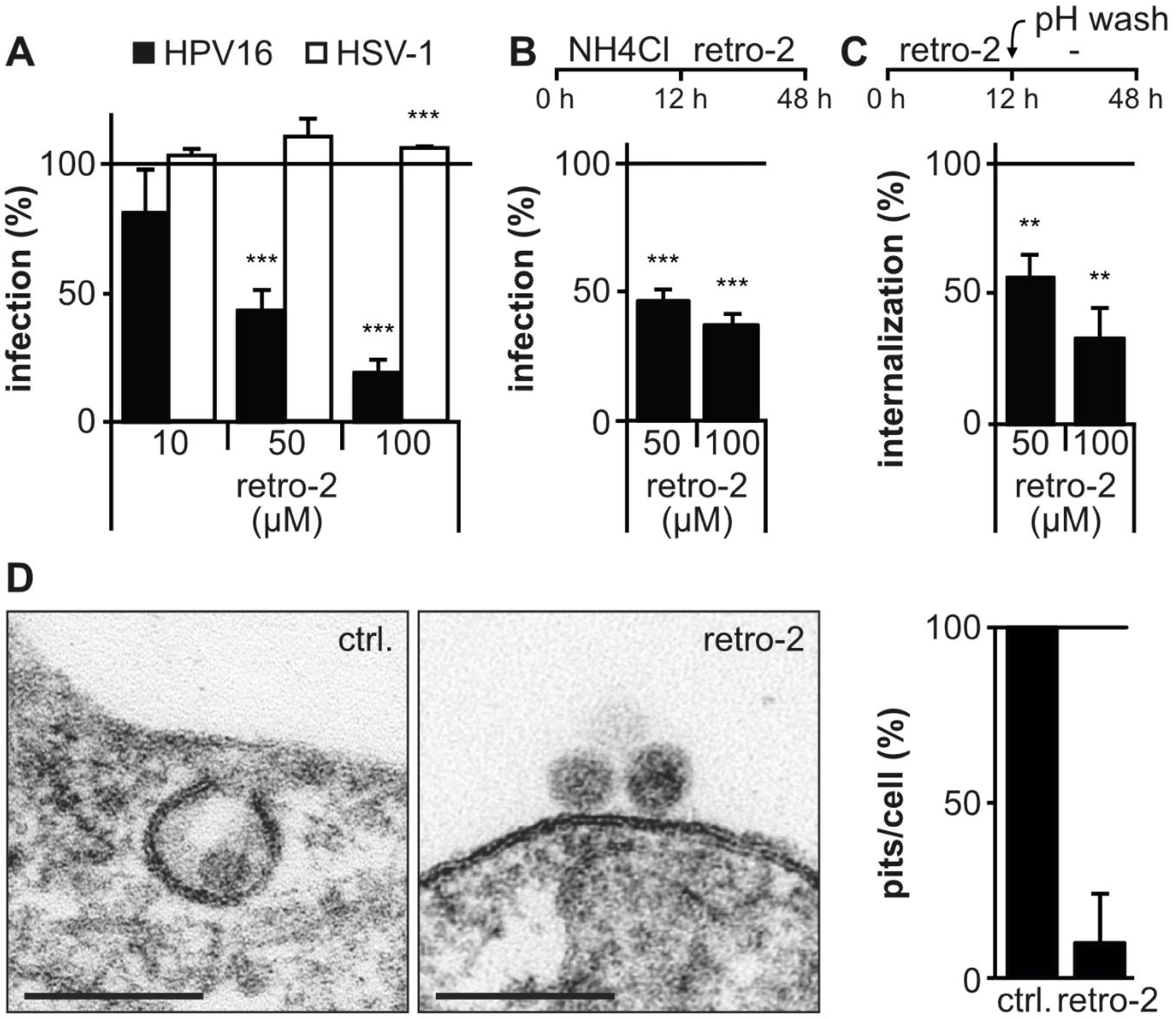
A
HPV16
HSV-1
infection (%)
100
50
0
***
***
***
***
10
50
100
retro-2
(µM)
B
NH4Cl
retro-2
0 h
12 h
48 h
infection (%)
100
50
0
***
***
50
100
retro-2
(µM)
C
retro-2
pH wash
-
0 h
12 h
48 h
internalization (%)
100
50
0
**
**
50
100
retro-2
(µM)
D
ctrl.
retro-2
pits/cell (%)
100
50
0
ctrl.
retro-2

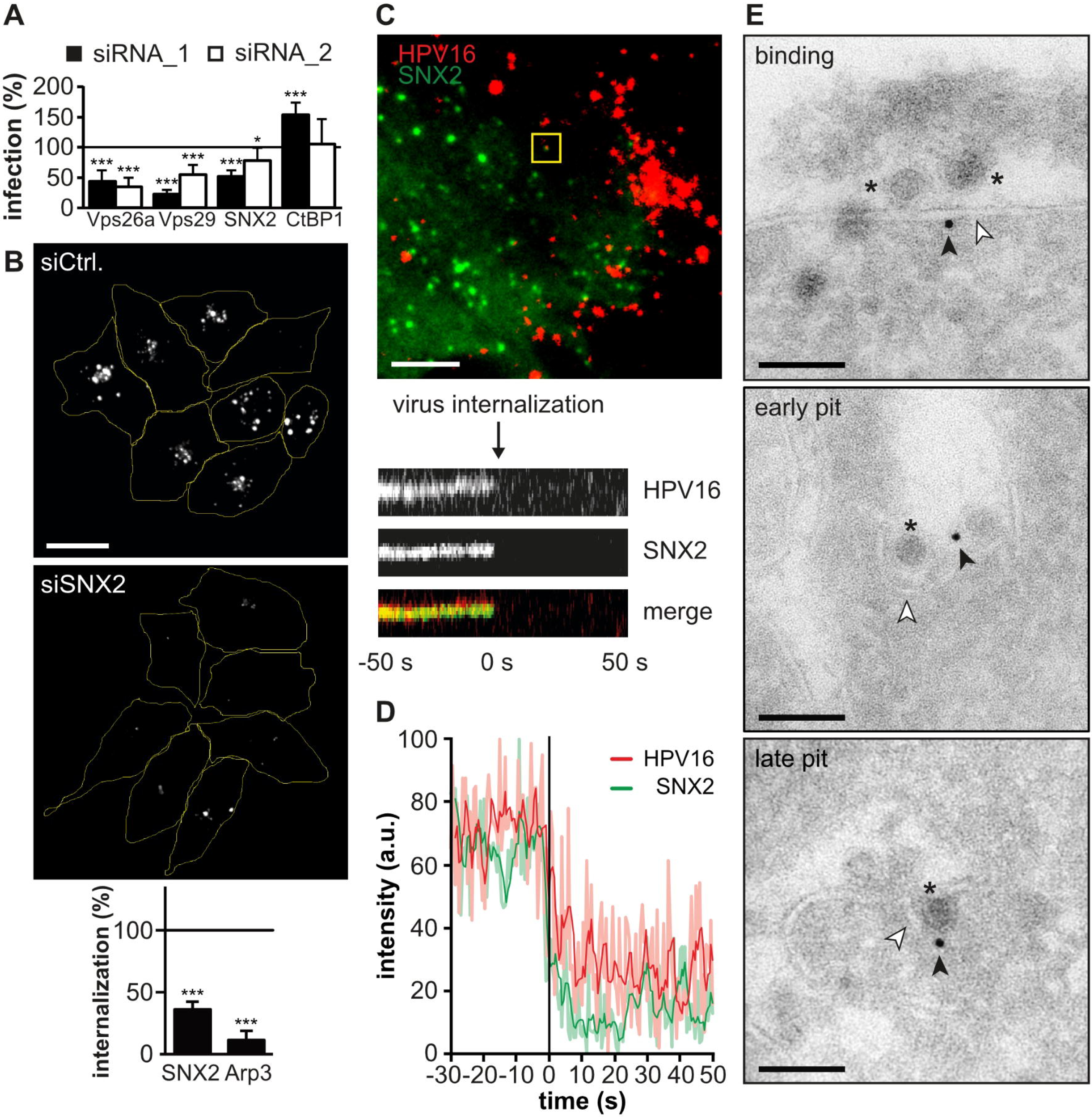
A
siRNA_1
siRNA_2
infection (%)
200
150
100
50
0
***
***
***
***
***
*
***
Vps26a
Vps29
SNX2
CtBP1
B
siCtrl.
siSNX2
internalization (%)
100
50
0
***
***
SNX2
Arp3
C
HPV16
SNX2
virus internalization
HPV16
SNX2
merge
-50 s
0 s
50 s
D
intensity (a.u.)
100
80
60
40
20
0
HPV16
SNX2
-30
-20
-10
0
10
20
30
40
50
time (s)
E
binding
*
*
early pit
*
late pit
*

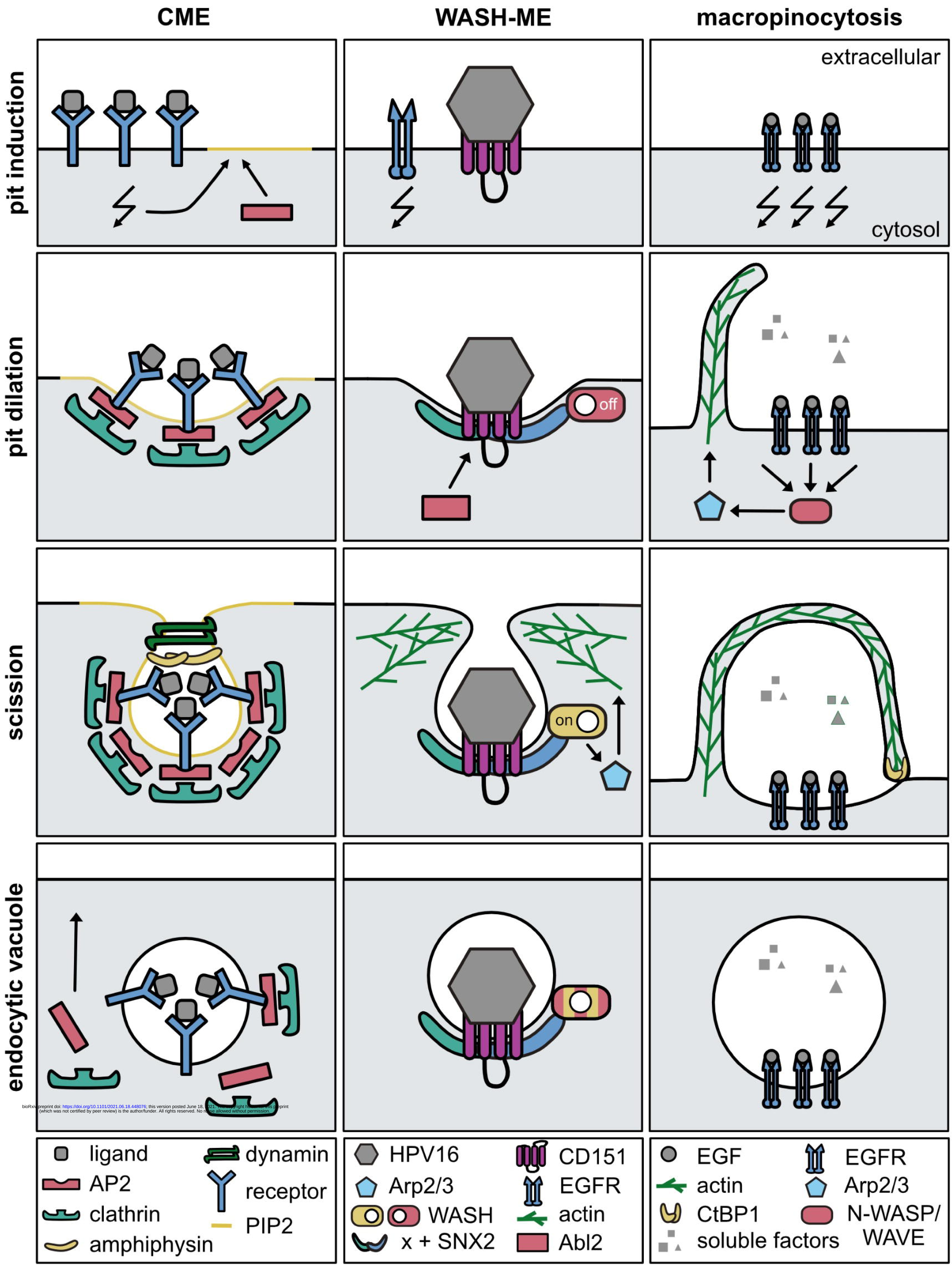
CME
WASH-ME
macropinocytosis
pit induction
pit dilation
scission
endocytic vacuole
extracellular
cytosol
off
on
ligand
AP2
clathrin
amphiphysin
dynamin
receptor
PIP2
HPV16
Arp2/3
WASH
x + SNX2
CD151
EGFR
actin
Abl2
EGF
actin
CtBP1
soluble factors
EGFR
Arp2/3
N-WASP/
WAVE